STRATOSPHERIC TRANSPORT CHANGES FORCED BY TROPICAL SEA SURFACE TEMPERATURE PERTURBATION: IDEALIZED SIMULATION

A Thesis

Presented to the Faculty of the Graduate School

of Cornell University

in Partial Fulfillment of the Requirements for the Degree of

Master of Science

by

Huang Yang

January 2013

ABSTRACT

The structure of mass transport in the stratosphere, as well as its dynamic behaviors, is explored by imposing idealized sea surface temperature (SST) perturbations in an aqua-planet model. Mass transport within stratosphere is simultaneously running through two processes: the diabatic circulation, also well known as the Brewer-Dobson Circulation (BDC), advecting air mass across isentropic surfaces, and the quasi-horizontal mixing ventilating air mass along isentropic surfaces. It is shown that, with an equatorial SST heating, the stratospheric transport will increase in strength, in a circumstance with both BDC and high-latitude isentropic mixing being accelerated. Behaviors of transport, for both BDC and isentropic mixing, turn out to be with more complexities when the imposed SST perturbation being relocated at different ranges of latitudes or expanding itself with larger longitudinal span. Dynamic diagnostics further relate the changes of stratospheric transport mainly to the changes of eddies, which are originated from the induction of SST perturbation.

BIOGRAPHICAL SKETCH

Huang Yang was born in downtown Changsha City, Hunan, China and graduated from Yali Middle School, a well-known local educational institute first founded by Yale University back in 1906. During his school years, he found his interest in earth sciences and potential in physics. That becomes his initial motivation to pursue an academic career in the Atmospheric Sciences, an interdisciplinary field with both his beloved two subjects deeply involved. Upon graduation from high school, he enrolled at the Nanjing University in the School of Atmospheric Sciences and earned a Bachelor Degree of Science in Meteorology through four years of study there. At his senior year, he got the opportunity to work with Dr. Ming Bao to investigate the remote forcing, from the Indian Ocean, on the anomalies in the East-Asia monsoon in a case of summer 1991. This research helped him attain a basic understanding about large-scale Climate Dynamics as well as strengthen his belief to devote himself further onto this amazing subject. During the same time, he applied and was very luckily accepted by the Department of Earth and Atmospheric Sciences at Cornell University. After the summer 2010, he flew half of the hemisphere to reach town of Ithaca, and worked as a graduate student with Dr. Gang Chen afterwards on the project of stratospheric mass transport, which turns into the topic of this thesis.

To Mom and Dad, who raised me up in all the ways as they can. And to my old neighbor and lifelong friend, Ms. Mei Yuan, who opened a young boy‘s heart to geosciences by a gift of globe at his tenth birthday.

ACKNOWLEDGEMENTS

I would like to acknowledge, particularly, the patient guidance from my adviser Dr. Gang Chen. It is him who led me into this spectacular field of climate dynamics on upper troposphere and lower stratosphere (UTLS) and walked all the way with me reaching here at this point. I would also like to thank my special committee members Drs. Stephen Colucci and Peter Hess. Prof. Colucci attended the weekly reading group, offered a wide variety of ideas and comments for my research, and Prof. Hess's class taught me a lot of stuffs about *Atmospheric Chemistry*, which potentially provides new scope of extension for my current study.

I also would like to acknowledge Dr. Lantao Sun and Dr. Qi Tang for their helps on my endless technique problems. And thanks to all my fellow graduate students (or undergrads) Michael Kelleher, David Alex Burrows, Aaron Perry, Yun Zheng, Wenxiu Sun, Rachel Scanza, Flora Min, Andrew Montreuil, Stephen Jessup and Marcus Walter for your supports and efforts making our office a wonderful place for both research and recreation.

Of course, mom and dad, always be the people I should appreciate most.

TABLE OF CONTENTS

LIST OF TABLES

LIST OF FIGURES

CHAPTER 1

INTRODUCTION

Since 1970s, a heated discussion on polar ozone depletion observed in Southern Hemisphere (SH) spring has drawn both public and climatologists into the vast stratosphere. In order to track the ozone depletion and to project future stratospheric ozone changes, it is crucial to understand the structure of mass transport in the stratosphere, including the one from upper troposphere into stratosphere. On the other hand, tropical ocean is a critical influential factor that could significantly affect the mass transport in both troposphere and stratosphere. Hence, it is important to test stratospheric transport responses by giving a certain tropical ocean forcing — set by sea surface temperature (SST) perturbation — in this study, especially when considering current increasing variability of the tropical ocean under a background of global climate change. In addition, given the ozone concentration, as well as its depletion, peaks at a height of 20-30 km (approximately 10 to 100 hPa), we particularly highlight the variation in the lower stratosphere in current study.

Generally, two processes synchronize to accomplish the mass transport in the stratosphere (see Haynes and Shuckburgh 2000a, Figure 1): one is the diabatic circulation, also well known as the Brewer-Dobson Circulation (BDC, Brewer 1949, Dobson 1956), conveying air mass across isentropic surfaces; the other is the eddy mixing exchanging air mass, primarily in a quasi-horizontal direction, along isentropic surfaces.

For BDC, it is a congregation of several overturns extending into different altitudes through the entire stratosphere, generally with ascends in the deep tropics and descends at middle and high latitudes. In its lowermost cell lying within

the lower stratosphere, the tropical tropopause upwelling (TTU) acts as the primary path for troposphere-to-stratosphere mass transport and hence becomes critical for stratospheric chemistry by setting its boundary conditions (Availone and Prather 1996, Butchart and Scaife 2001, Olsen et al. 2001, Austin et al. 2007, Li et al. 2009). Model studies documents that this TTU tends to be intensified under scenarios of both current global warming (Garcia and Randel 2008), induced by greenhouse gases (GHG) accumulation, and increasing El-Niño events (Calvo et al. 2010, Simpson et al. 2011). And this acceleration is confirmed by radiosonde observations showing a cooling trend of tropical tropopause temperature (an indicator of intensity of TTU, Thompson and Solomon 2005, Fu et al. 2010). However, by measuring the age of stratospheric air, airborne balloon trace gases observations, embedded with uncertainties, indicate a steadiness in the strength of BDC during past decades (Engel et al. 2008), which is contrary to the results from most model simulations (Waugh 2009). Another key feature about the TTU and associated BDC is: they are wave driven (Haynes et al. 1991, Holton et al. 1995). Yulaeva and Holton (1994), Ueyama and Wallace (2010) utilized this mechanism to interpret the seasonal cycle of tropical tropopause temperature and attached it with the seasonal cycle of extratropical wave forcing by establishing a strong temporal connection between them. However, Plumb and Eluszkiewicz (1999) proposed the tropical upwelling cannot be detected until the wave forcing extends sufficiently close to the equator. Therefore, enhanced extratropical waves only cannot explain a robustly strengthened upwelling in deep tropics. Later studies (Kerr-Munslow and Norton 2006, Norton 2006, Deckert and Dameris 2008) unveil the importance of equatorial wave drags induced by latent heat release from deep convection. Further, Randel et al. (2008) summarized that the current intensification of TTU is a combined ef-

fect attributed to both equatorial waves and extratropical synoptic waves. And the variation of these waves under climate change is projected by Garny et al. (2011), including the one associated with the oceanic SST perturbation.

While BDC advects air mass from tropics into polar region through long distance, mixing occurs locally, in a relative sense, exchanging air mass between adjacent regions along the isentropic surfaces. In nature, mixing not only helps to build a secondary connection between upper troposphere and lower stratosphere, but also contributes to the formation of 'surf zone' in mid-latitude stratosphere, in which substance concentration remains relatively uniform. Meanwhile, mixing is effected directly through wave breaking (Haynes and Shuckburgh 2000b), which could also be significantly influenced by a SST perturbation over the ocean.

With current climate change, encompassing the feedback from tropical ocean, both BDC and mixing would adjust themselves into a new balance state, and subsequently modify the structure of stratospheric mass transport. Although both BDC and mixing are highly linked to the waves originated from climate forcing (e.g. SST), the critical influential region and mechanisms wjthin each process vary spatially in terms of latitudes and altitudes. The relative independence between these two processes hence enable us to evaluate their contribution to the mass transport in the stratosphere separately, by systematically imposing the SST perturbation in idealize simulation and observing how the synthetic transport changes can be decomposed into different variation of BDC and isentropic eddy mixing.

Through this study, it is motivated to answer the following three questions: (a) how will the stratospheric transport vary with a SST perturbation, and how

much portion of the variation in transport is attribute to the BDC and isentropic eddy mixing respectively; (b) once the SST perturbation has been relocated or reshaped, how would the BDC, mixing and stratospheric transport respond then; (c) what are the driving factors of the variation and which one dominates, in which way and occasion. In order to approach these goals, the model and methods applied in this study are briefly described in Chapter 2. With a standard two-dimensional Gaussian SST perturbation centered at the equator, the corresponding atmospheric responses are given in Chapter 3, with a highlight on the changes of BDC, mixing and mass transport. Chapter 4 focuses on the dynamic factors beneath the variation of BDC and isentropic mixing. Multiple methods are performed to physically interpret the driving mechanism of changes of TTU in both a zonal mean sense and a zonal asymmetric sense. A brief reasoning on the connection between wave breaking and isentropic mixing is also introduced. Through this chapter, a panoramic view on the physical mechanism, through which the TTU is triggered and isentropic mixing occurs, is presented. Chapter 5 extends this study further by applying different types of SST perturbation in terms of varying heating center latitude or longitudinal span, shows differed atmospheric responses correspondingly, and discusses in details: why the variation of BDC, isentropic mixing and stratospheric transport will change after the latitude of heating center being moved, or span being enlarged longitudinally. In addition, the critical zones for BDC and isentropic eddy mixing impacts are also identified in this chapter. Further discussion and conclusion are given in Chapter 6 and Chapter 7 respectively.

CHAPTER 2

METHODOLOGY

2.1 Model

The model applied here is the Geophysical Fluid Dynamics Laboratory (GFDL) Aqua-planet model version 2.1 (Delworth et al. 2006). It has a horizontal resolution of approximately 2.5° (longitude) by 2° (latitude) and an upgraded vertical resolution from a 24 levels low top scheme to 48 levels with a much higher top layer close to 0.01 hPa. This upgrade in the vertical resolution significantly improves the computational precision and the subsequent physical balances in simulating stratospheric processes. The model itself is an idealized version of a typical full Atmospheric General Circulation Model (AGCM), but there are still several differences worthy of noting: (a) no ice and associated radiation-convection processes are considered in this model; (b) topography is turned off making the earth into a symmetric spherical planet fully covered by liquid water. As a result, no external gravity waves are generated in the model (as to internal gravity waves, the resolution of model is insufficient to resolve them). Inclusion of all other physical processes enables the model to simulate the responses of stratospheric transport to a surface heating more elaborately and consequently avoid drastic unreality, which are commonly seen in some simple dry dynamic models (Norton 2006). On the other hand, certain assumptions and idealizations act to physically sift signals generated by some very complicated feedbacks and make the primary physical processes easier to be detected while diagnosing. Hence, such a setting of model is qualitatively a good start to examine SST-forced transport changes and it is also the major reason for being

chosen in current study.

As to SST, the only changing external forcing in this study, its flexibility of variation enable us to systematically examine the sensitivity of stratospheric mass transport to the changes of SST perturbation. For sensitivity experiment, a control run is required and here it is prescribed by applying a method analogous to Neale and Hoskins (2000). As illustrated in Figure 2.1, the control run is generated with a zonal-asymmetric Gaussian-like SST forcing shown mathematically as Equation 2.1. Named as *Qobs* (abbreviated for quasi observation), it basically resembles the annual-mean global surface temperature profile giving a warm peak at the equator and two cold wells at the poles. Further, a standard two-dimensional Gaussian distributed temperature anomaly is added onto the original prescribed SST in the control run resulting in a comprehensive SST heating shown as the middle panel of Figure 2.1. Following Equation 2.2 and 2.3, a set of different experiments are formed by altering the heating center latitude ϕ_0 or heating longitudinal span λ_S. Apparently, these elliptic hot bubbles look analogous to the warm El-Niño - Southern Oscillation (ENSO) SST anomalies, so we are expecting to detect some resemblances by comparing results derived from present model simulations with realistic observations during those warm ENSO events. Other properties of SST forcing, like size, sign and intensity, can all be modified in the model for future research purposes. Details on the parameter settings for all simulations can be found on Table 2.1 (also graphically represented as Figure 2.2).

$$T_{ctrl} = 27 \times \left(\frac{1}{2} \sin^2 \phi' + \sin^4 \phi' \right) \tag{2.1}$$

where $\phi' = \max\left(\min\left(\frac{3}{2}\phi, \frac{\pi}{2}\right), -\frac{\pi}{2}\right)$ and ϕ is the latitude.

Table 2.1: SST settings in all simulations with parameters specifying intensity, location of heating center, latitudinal and longitudinal range of anomalous heat forcing.

Name	Intensity	Heating Center		Heating (e-folding) From the Center	Span Apart
	Gaussian (I_G)	Longitude (λ_0)	Latitude (ϕ_0)	Longitude (λ_S)	Latitude (ϕ_S)
Qobs	0	N/A	N/A	N/A	N/A
Qobs_3gau	+3K	180°	0	30°	15°
Qobs_3gau_5N			5°N		
Qobs_3gau_10N			10°N		
Qobs_3gau_15N			15°N		
Qobs_3gau_20N			20°N		
Qobs_3gau_25N			25°N		
Qobs_3gau_30N			30°N		
Qobs_3gau_X15			0	15°	
Qobs_3gau_X60			0	60°	
Qobs_3gau_X90			0	90°	
Qobs_3gau_X150			0	150°	
Qobs_3ygau			0	∞	

$$T_{anmly} = I_G \times \exp\left[-\left(\frac{\lambda - \lambda_0}{\lambda_S}\right)^2 - \left(\frac{\phi - \phi_0}{\phi_S}\right)^2\right] \tag{2.2}$$

$$T_{surf} = T_{ctrl} + T_{anmly} \tag{2.3}$$

Here, the European Center for Medium-Range Weather Forecast (ECMWF)

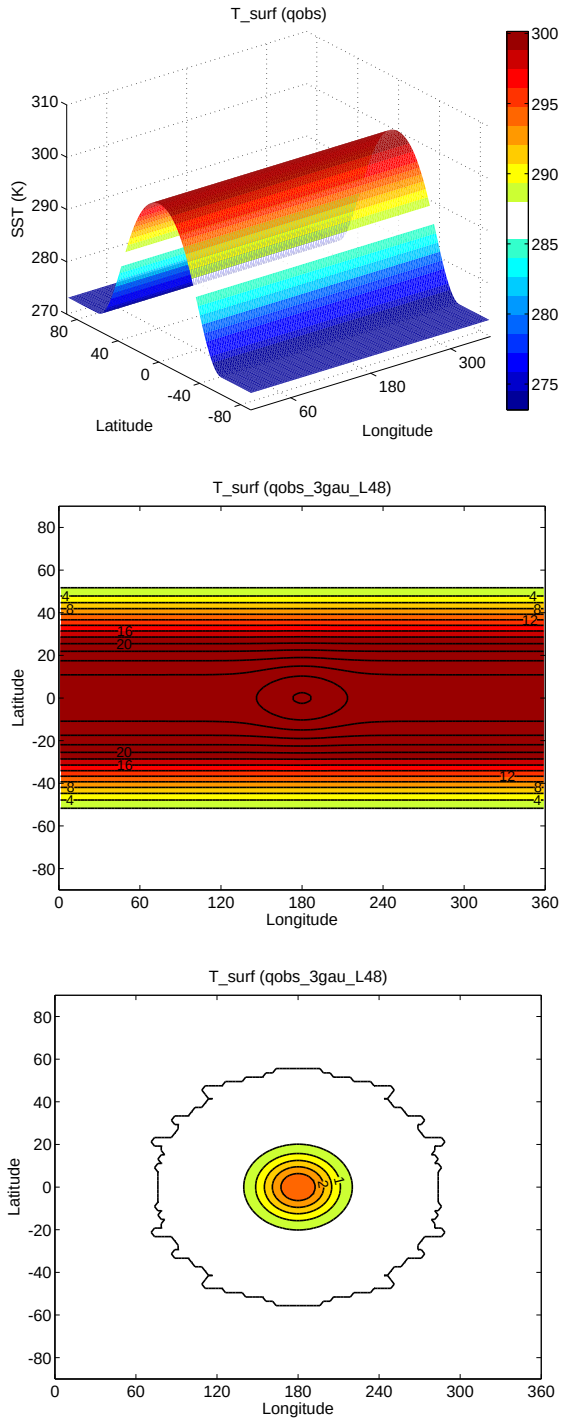

Figure 2.1: SST settings in the study for: (top) control run *Qobs* (units: K); (middle) experimental run *Qobs_3gau* (units: °C, i.e. above 273K). (bottom) The net two-dimensional Gaussian-shaped perturbation in *Qobs_3gau* with heating center at the equator (units: K).

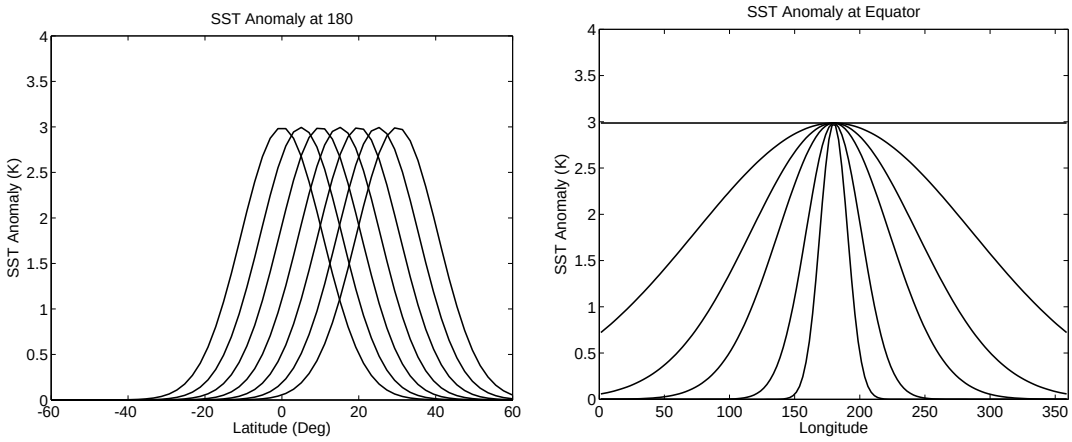

(a) (b)

Figure 2.2: SST perturbation (units: K) in the study for: (a) Gaussian perturbation experiments, with fixed $\lambda_S = 30^\circ$ and varied heating center latitude ϕ_0, in a longitudinal cut at 180°. Notice that the heating center latitude ϕ_0 shifts gradually from the equator to 30°N with a 5° interval; (b) Gaussian perturbation experiments, with fixed heating center latitude at the equator (i.e. $\phi_0 = 0$) and varied heating longitudinal span λ_S, plotted along the equator. Notice that the heating longitudinal span λ_S varies from 15° to 30°, 60°, 90°, 150° and ∞ respectively, generating the equatorial SST perturbation longitudinally broader and broader.

ERA-40 reanalysis data (Uppala et al. 2005) has been utilized to testify the validity of the model in terms of atmospheric responses with SST perturbation noted above. From Figure 2.3, by comparing the total field of certain meteorological properties derived from reanalysis data with the one from model control run *Qobs*, it is clear that current GFDL aqua-planet model successfully captures the most substantial characters of nature. For zonal mean zonal wind, though unrealistically over two times stronger in magnitude, subtropical jets are established in the model with almost identical latitudinal locations centered at ±40°. Polar night jets are also built in the stratosphere, with a slightly poleward shift though. Easterlies prevail in the tropical stratosphere in the model as they do in nature. However, the monotonically growth of wind speed with altitude

in the model makes the simulated easterlies weaker than reality in the lower stratosphere but stronger when it goes higher. As to temperature field, though steeper downward isotherms are found in the simulation close to poles, temperature configuration in the (sub)tropics is identical to what derives from ERA-40 reanalysis, particularly the cold pool of lower than 210K is clearly seen at the tropical tropopause. At last, residual stream function are calculated (definition see Equation 3.1) denoting the general structure of stratospheric BDC. Obviously, the hemispherically extended one cell configuration is discernible in both model simulation and observation, demonstrating the consistency between the model and reality in simulating stratospheric processes.

All experiments are set to run for 14 years starting from the same initial condition at 1982, except the SST. The first-year data have been removed to diminish spin-up effects. The time step of the model is 20 minutes, but in a compromise between keeping diurnal information and saving storage space, the output frequency is set to be four times daily for all daily-output variables in all experiment sets. These high frequency instantaneous outputs are used to estimate tendencies, fluxes and further calculate stream functions in a physically satisfactory quality. Note that the output for the potential vorticity and tracer mixing ratio are added after 1985. Hence, the analysis involving these two quantities are based on the data from 1986 to 1995, ten years in total. On the contrary, all other analysis without interfering with these two quantities are labeled with the data before 1986 since the other quantities in the model stabilize quickly after approximately one year and will not change their climatology state significantly by simply elongating the running time of simulation. In addition, shown as Equation 2.4, the model is established vertically on the Sigma level coordinates through dividing in situ pressure by the the surface pressure p_S right below, but

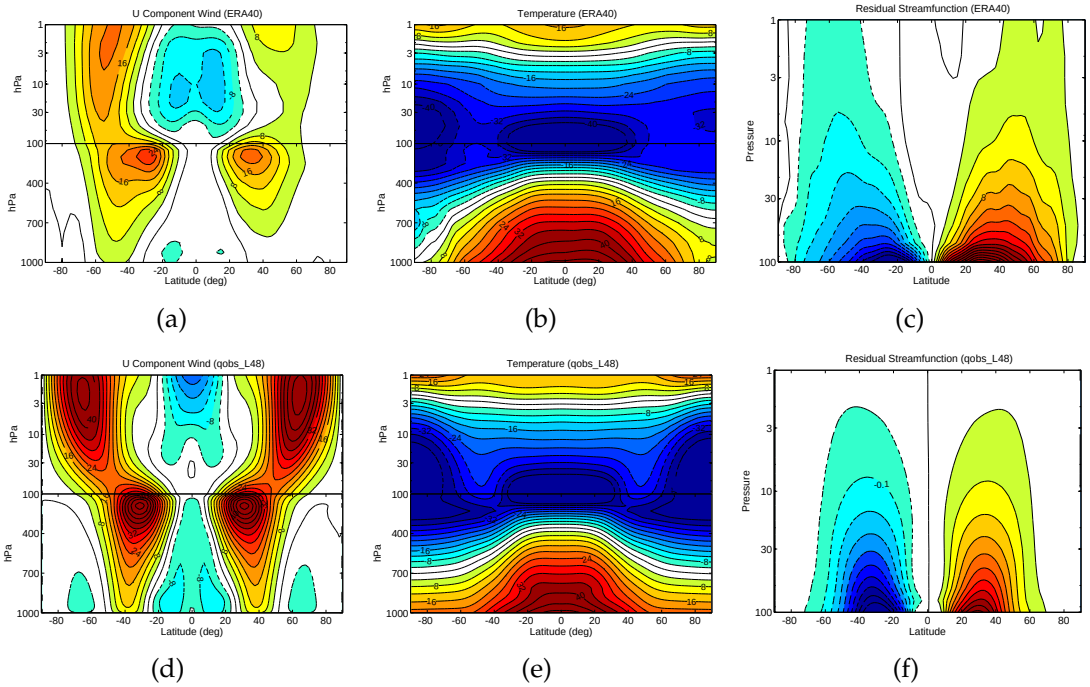

Figure 2.3: Comparison between two datasets from ECMWF ERA-40 reanalysis (top row (a)(b)(c)) and model simulation *Qobs* (bottom row (d)(e)(f)) respectively, in terms of: (a)(d) zonal mean zonal wind $\bar{u}$ (unit: m/sec, interval: 4 m/sec); (b)(e) zonal mean temperature $\bar{T}$ above 250 K (unit: K, interval: 4 K); (c)(f) residual stream function $\bar{\chi}^*$ (refers to Equation 3.1) in the stratosphere (unit: $10^9\,\mathrm{kg\,sec^{-1}}$, interval: $2 \times 10^9\,\mathrm{kg\,sec^{-1}}$ in (c) and $0.05 \times 10^9\,\mathrm{kg\,sec^{-1}}$ in (f)).

the diagnostic methods applied later (see Section 2.2 for details) are based on pressure coordinates or log-pressure coordinates. Hence theoretically, an interpolation of data from Sigma level to pressure level is prerequisite. However, in order to save computation resources, a pseudo-pressure coordinate is defined by simply setting surface pressure p_S as 1000 hPa everywhere over the model domain.

$$\sigma(\lambda, \phi) = \frac{p(\lambda, \phi)}{p_S(\lambda, \phi)} \tag{2.4}$$

For experiment *Qobs* and *Qobs_3gau*, it has been shown that analysis basing on such a pseudo-pressure coordinates have no significant differences with those derived from the interpolated pressure coordinates (not shown here). Still, neglecting the spatial variation of surface pressure p_S completely might not be reasonable at specific occasion. As a result, referring to the dynamic equations in Sigma level coordinates, the momentum flux in this study is specifically calculated as Equation 2.5.

$$\overline{v'u'} = \frac{\overline{(p_S v)' u'}}{\bar{p}_S} \tag{2.5}$$

Here, u, v are zonal and meridional component of velocity respectively. An overbar ahead certain property denotes the zonal mean of the property and the prime denotes the departure of the property from its zonal mean. Hence, $\overline{v'u'}$ is the momentum flux and the definition here helps us to analyze simulation outputs in current pseudo-pressure coordinate with mathematical diagnostic methods for pressure coordinates without significant computational departure.

Subsequently, all data, including post-emerging ones like fluxes, are applied with a temporal average operator to obtain the climatology state (termed as the total field for each property) in each experiment. Analogous to SST setting, to define the anomaly field of each property in each experiment, its total field value in the control run is subtracted from the total field value from that specific perturbation experiment. For example, the anomaly of temperature in *Qobs_3gau* is procured following $T_{anmly}\,(Qobs\_3gau) = T\,(Qobs\_3gau) - T\,(Qobs)$. It is exactly these anomaly fields interpreting the atmospheric responses above an anomalous SST heating and becoming what being focused in present study.

2.2 Diagnostic Methods

2.2.1 Transformed Eulerian Mean Circulation

The BDC in the stratosphere is very slow, with a speed in an order of millimeter or less ($10^{-4} - 10^{-3}$ m). Therefore, the air mass transported by it takes quite long from place to place and the conventional Eulerian measurement is no longer appropriate in quantifying the BDC. The Lagrangian measurement is a decent approach in evaluating the transport effects by BDC, which has a timescale of years, but the mathematical description for such perspective is much more inconvenient to use. As a result, considering the stratospheric Lagrangian circulation outside deep tropics is primarily effected by eddies (Gerber 2012), the Transformed Eulerian Mean (TEM) theorem is commonly induced in the study of stratosphere (Edmon Jr et al. 1980, Andrews et al. 1987). By applying the TEM theorem, the Lagrangian circulation can be effectively detected and described as the residual circulation using the conventional Eulerian measurement. Specifically, the horizontal and vertical component of residual velocity in a residual circulation are defined in Equation 2.6.

$$\bar{v}^* = \bar{v} - \frac{\partial}{\partial p}\left(\frac{\overline{v'\theta'}}{\bar{\theta}_p}\right) \tag{2.6a}$$

$$\bar{w}^* = \bar{w} - \frac{1}{\rho_0 g a \cos\phi}\frac{\partial}{\partial \phi}\left(\cos\phi\frac{\overline{v'\theta'}}{\bar{\theta}_p}\right) \tag{2.6b}$$

Herein, ϕ, p, a and ρ_0 denote the latitude, pressure altitude, radius of the Earth and zonal mean density respectively. θ stands for the potential temperature and its vertical derivative θ_p provides an indicator for atmospheric stability. Conse-

quently, the momentum balance, mass balance and energy balance should all be reconstructed once the residual circulation is induced, and they are shown as Equation 2.7.

$$\bar{u}_t - \hat{f}\bar{v}^* - \bar{X} = \mathbf{DF} \tag{2.7a}$$

$$\frac{1}{a\cos\phi}\frac{\partial}{\partial\phi}\bar{v}^*\cos\phi + \frac{\partial\bar{\omega}^*}{\partial p} = 0 \tag{2.7b}$$

$$\bar{\theta}_t + \bar{\omega}^*\frac{\partial\bar{\theta}}{\partial p} - \bar{Q} = 0 \tag{2.7c}$$

$\bar{u}_t$ represents the zonal mean zonal wind tendency while $\bar{X}$ encompasses the wind tendency induced by all other parameterized physical processes in the model, say like friction induced by Rayleigh sponge layer at the model top. $\bar{\theta}_t$ denotes the potential temperature tendency and $\bar{Q}$ denotes the diabatic heating in the simulation, such as latent heat release, cloud radiation and etc. $\hat{f}$ is the modified Coriolis parameter and $\hat{f} = f - (1/a\cos\phi)(\partial/\partial\phi)(\bar{u}\cos\phi)$. $\bar{\omega}^*$ is the residual vertical velocity in a *pressure* coodinate and it can be converted to $\bar{w}^*$ in the *log-pressure* coordinate defined in Equation 2.6 following the hydrostatic balance $\bar{w}^* = -\frac{\bar{\omega}^*}{\rho_0 g}$ (The assumption of hydrostatic balance is valid in current research for large-scale atmospheric systems discussion). At last, there is an very important term in the momentum balance in this TEM theorem — the Eliassen-Palm (EP) flux divergence (**DF**). It is mathematically defined by following Equation 2.8 and 2.9.

$$\begin{aligned}\mathbf{DF} &= \frac{1}{a\cos\phi}\nabla\bullet\mathbf{F} \\ &= \frac{1}{a\cos\phi}\left[\frac{1}{a\cos\phi}\frac{\partial\left(F_\Phi\cos\phi\right)}{\partial\phi} + \frac{\partial F_p}{\partial p}\right]\end{aligned} \tag{2.8}$$

where **F** is the EP flux vector with components as

$$F_{\Phi} = a\cos\phi\left[-\overline{v'u'} + \left(\frac{\partial\bar{u}}{\partial p}\right)\frac{\overline{v'\theta'}}{\bar{\theta}_p}\right] \tag{2.9a}$$

$$F_p = a\cos\phi\left[\hat{f}\frac{\overline{v'\theta'}}{\bar{\theta}_p} - \overline{\omega'u'}\right] \tag{2.9b}$$

Here, $\overline{v'u'}$, and $\overline{\omega'u'}$ are the horizontal and vertical momentum flux respectively. The importance of this EP flux quantity will be discussed in details in Section 4.1.1. In all aspects, the TEM theorem provides the physical framework in which the stratospheric circulation decides its dynamic and thermodynamic behaviors, and further can be used to disentangle critical driving factors individually from the complicated atmospheric responses commonly observed in the stratosphere.

2.2.2 Downward Control and Thermodynamic Balance

One of the application of the TEM theorem is the 'downward control' principle (Haynes et al. 1991) and it has been applied in many studies about BDC (Garcia and Randel 2008, Randel et al. 2008, Calvo et al. 2010, Garny et al. 2011). In order to achieve the momentum and continuity balances, the residual vertical velocity in *log-pressure* coordinates, as denoted in Equation 2.10, is highly determined by the source of wave forcing (represented by the EP flux divergence, **DF**) above the layer of interest.

$$\left\langle \bar{w}^*_m \right\rangle (p) = -\frac{1}{\rho_0(p)\, g \int_{\Phi_1}^{\Phi_2} a\cos\phi\,\mathrm{d}\phi}\left\{-\cos\phi\int_p^0 \frac{p'\left[\mathbf{DF}(\phi,p') - \bar{u}_t - \bar{X}\right]}{\hat{f}(\phi,p')}\,\mathrm{d}\ln p'\right\}_{\Phi_1}^{\Phi_2} \tag{2.10}$$

Curly bracket here interprets the subtraction operation of the quantity inside at latitude Φ_1 from the one at latitude Φ_2, and this helps the computation skip small Coriolis effect when approaching the equator. Note the prime in Equation 2.10 does not mean departure after zonal averaging, it is just another form of property p specified as the integration variable.

On the other hand, $\bar{w}^*$ can be also derived from the thermodynamic balance (the term of meridional gradient of temperature turns out to be trivial and it is neglected here) shown as Equation 2.11.

$$\bar{w}^*_Q = -\frac{1}{\rho_0 g}\frac{\bar{Q}(\theta, p)}{\bar{\theta}_p} \tag{2.11}$$

$\bar{w}^*_m$ is the residual vertical velocity derived from the momentum balance and $\bar{w}^*_Q$ is the one derived from the thermodynamic balance. Theoretically, they should be both numerically equivalent to $\bar{w}^*$ deduced from definition, and so the exact coherence represents how much the vertical velocity, particularly within TTU, is wave driven and how much it is consistent with the diabatic heating adjustment.

2.2.3 Vorticity Balance

Moreover, the variation of TTU is a relatively localized phenomenon (shown in Section 4.1.2) and is characterized with pronounced zonal asymmetry. Established on the TEM theorem, the downward control principle can no longer serve as an effective tool while exploring in a full three-dimensional scope. Instead, the vorticity equation has been taken into consideration. By checking the

balance between vorticity advection and vorticity-divergence product, Norton (2006) applied Equation 2.12 to diagnose the variation of TTU under idealized tropospheric heating.

$$\frac{\partial \zeta_a}{\partial t} + \mathbf{V}_\psi \bullet \nabla \zeta_a + \mathbf{V}_\chi \bullet \nabla \zeta_a + \zeta_a \nabla \bullet \mathbf{V} = 0 \tag{2.12}$$

Here ζ_a is the absolute vorticity, encompassing the planetary and relative components. Velocity field $\mathbf{V}$ has been decomposed into the divergent wind $\mathbf{V}_\chi$ and non-divergent wind $\mathbf{V}_\psi$ respectively. And this method is also used in the zonal asymmetry analysis of current study to qualitatively interpret the variation of TTU after imposing the SST perturbation.

2.2.4 Equivalent Length

For eddy mixing along isentropic surfaces noted in Chapter 1, Nakamura (1996) has developed the 'equivalent length' (L_e) to quantify it.

$$L_e^2 = \frac{\partial}{\partial A} \iint\limits_{A(q,t)} |\nabla q|^2 \, dA \Big/ \left(\frac{\partial q}{\partial A} \right)^2 \tag{2.13}$$

Here, q is the magnitude of tracer, and A is the area within which q exceeds a certain value q_0. Note the integral follows the tracer contours, which is a Lagrangian perspective of measurement, instead of the conventional zonal measurement in the Eulerian system. Generally, the equivalent length is a quantity assessing the twisting extent of tracer contours. The longer the equivalent length L_e is, the more the tracer contour has been twisted, and certainly

lies more possibility for eddy mixing with larger stretching rate. Moreover, the tracer used in the calculation could be anything that is qualitatively conservative within the timescale we concerned. For instance, it could be the mixing ratio of certain chemical species possessing long lifetime in the stratosphere like SF_6 and CO_2, or even potential vorticity, a dynamic quantity which is conservative along isentropic surfaces. In current study, the Ertel Potential Vorticity (EPV) is chosen as the tracer and it is defined as $q = -g\zeta_a \frac{\partial \theta}{\partial p}$. Note that we are analyzing isentropic eddy mixing here, so the EPV data needs first to be interpolated onto designated isentropic levels.

If the tracer contour circles the earth following exactly the the loop along longitudinal direction, then its equivalent length shrinks to the minimum — the length of that longitudinally headed loop L and $L = 2\pi a \cos\phi$ for a given latitude ϕ — and there would be no eddy mixing occurring along isentropic surfaces. Hence, the equivalent length ratio $\tilde{\kappa}_{eff} = L_e^2 / L^2$ provides a non-dimensional approach to evaluate the significance of isentropic eddy mixing regardless the difference of latitudes and it is the quantity we applied in current study. The larger $\tilde{\kappa}_{eff}$ is, the more isentropic eddy mixing occur. When $\tilde{\kappa}_{eff} = 1$, the isentropic eddy mixing is negligible.

2.2.5 Age of Air

In order to directly evaluate the effects of mass transport, a clock tracer has been input close to the bottom boundary of the model. Several sinks are set at the high top, which is sufficiently far away from the source. Thus, the clock tracer is conservative for most domain in the model. Further, due to a tem-

porally uniform release of the tracer, its mixing ratio, in those conservative regions, theoretically tends to increase linearly with time at an uniform growth rate. However, that does not mean the mixing ratio of the tracer in the model will increase uniformly everywhere. In fact, the tracer at points far away from the source will reach a certain level of mixing ratio obviously much later than the one at points close to the source. It is indeed this time lag that has been defined as the mean age of air (AOA) to quantify the speed of transport (Hall and Plumb 1994, Waugh 2009).

$$\Gamma = t(\chi; \phi, p) - t(\chi; \phi_0, p_0) \tag{2.14}$$

Γ is the mean AOA, χ the mixing ratio of the tracer. ϕ_0 and p_0 are latitude and pressure altitude at the reference point. Hence, the mean AOA at any given point is defined as the time lag for the tracer at this point reaching the same magnitude of mixing ratio as the one at the reference point (see Figure 1 in Waugh 2009). The reference point do not necessarily be constrained at the source. For most stratosphere research, it is chosen at the tropical tropopause in order to highlight the stratospheric transport. Here, we follows Garcia et al. (2011)'s scheme by calculating the mean AOA using monthly averaged mixing ratio of the clock tracer, and setting the reference point at $\phi_0 = 0$, $p_0 = 150\,\mathrm{hPa}$. It has been shown that the tracer becomes well mixed in the tropical troposphere with a timescale less than a month, so the current choice on reference point makes no significant difference with the one at the source. Morevoer, the mixing ratio of tracer usually will not follow exactly a linear growth with a precise uniform growth rate in practice, hence the AOA derived from Equation 2.14 will vary depending on the choice of mixing ratio level χ. In other words, for a time se-

ries of mixing ratio χ at any given point, there is a corresponding time series of AOA. Usually, this AOA series will vibrantly increase and then oscillate without significant trend for upwelling or downwelling (See Figure 2 in Garcia et al. 2011). It is the second steadily oscillating part that can lead us to the 'authentic' mean AOA. Therefore, for any given point, we first apply a ten-elements moving box (i.e. ten months) to smooth the time series of AOA, then regard the first point without climbing as the critical time spot, pick up the rest of time series, and average it to procure the mean AOA for this given point. The typical mean AOA in the stratosphere extends from months to tens of years, and it is the reason why the model needs to be run for a sufficient long time. Besides the mean AOA, its latitudinal gradient can be used to identify the transport barrier (Gerber 2012).

CHAPTER 3

ATMOSPHERIC RESPONSES WITH EQUATORIAL SEA SURFACE TEMPERATURE PERTURBATION

On a planet fully covered by liquid water in current simulation studies, the SST determines how much energy the earth is reemitting back into the atmosphere. Hence, any perturbation on the SST will act like an external force causing atmospheric changes in order to comply with the energy balance. Figure 3.1 illustrates such changes after imposing a Gaussian SST perturbation with a 3K peak centered at the equator (*Qobs_3gau*) noted in Section 2.1. Clearly, the zonal mean zonal wind is significantly strengthened right above the heating source in the deep tropics (cf. Figure 3.1(a)). With its maximum being greater than 17 m/sec at approximately 150 hPa, equatorial superrotation (Held 1999) is found (not shown here) and tends to induce favorable tunnel for stationary wave propagation which will be discussed in details in Section 4.1.1. Both subtropical jets in troposphere and polar night jets in the stratosphere are weakened in responses of the equatorial SST perturbation. This structural adjustment on the zonal flow will significantly affect the mass transport in many aspects, which will be further discussed later. Simultaneously over equatorial region, temperature increases in the upper troposphere and decreases as low as 4K in the lower stratosphere, with the zero isopleth aligned close to the tropopause (cf. Figure 3.1(b)). This spatial pattern qualitatively bears a similarity with the temperature anomaly field regressed onto the Multivariate ENSO Index (MEI) procured in Randel's work (Randel et al. 2009) by utilizing the adjusted Radiosonde Innovation Composite Homogenization (RICH) satellite data, which, in another approach, ascertains the validity of the model. Moreover, this tropospheric-warming-stratospheric-cooling pattern of tempera-

ture anomaly is consistent with the changes of diabatic heating shown in Figure 3.1(c). A detailed look at the diabatic heating budget (not shown here) shows that the longwave radiation adjustment accounts for most of stratospheric diabatic warming. Meanwhile, a combined variation from shortwave radiation, large-scale stratus clouds, and convection is responsible for the tropospheric diabatic cooling. With the anomaly field being contrary to the climatological total field, the Hadley Cell, indicated by the conventional Eulerian mean tropospheric stream function shown in Figure 3.1(d), has been weakened by exerting equatorial SST warming. Though the weakening tendency of the Hadley Cell is contrary to the results of many precedent literatures, for instance, Chen et al. (2010), they applied zonal symmetric heating, which is different from the Gaussian perturbation with zonal asymmetry here.

Particularly for the intensity changes of TTU above the equatorial Gaussian SST heating, Figure 3.2(a) shows directly an intensification of zonal mean vertical velocity $\bar{w}$ in deep tropics through the whole stratospheric column indicating a strengthening of TTU. It is consistent with the strengthening of the diabatic circulation in the stratosphere (cf. Figure 3.2(b)), denoted by the residual stream function with definition shown as Equation 3.1.

$$\bar{\chi}^{*}(p,\phi) = \int_{0}^{p} \frac{-2\pi a \cos\phi \, \bar{v}^{*}(p',\phi)}{g} \, \mathrm{d}p' \tag{3.1}$$

Moreover, the strengthening of BDC is consistent with the thermal structure adjustment in the stratosphere. (cf. temperature changes in Figure 3.1(b) and diabatic heating changes in Figure 3.1(c)). Specifically, due to the background stratospheric temperature increases monotonically with height, stronger TTU advects more cold air mass from the tropopause to relatively warm higher alti-

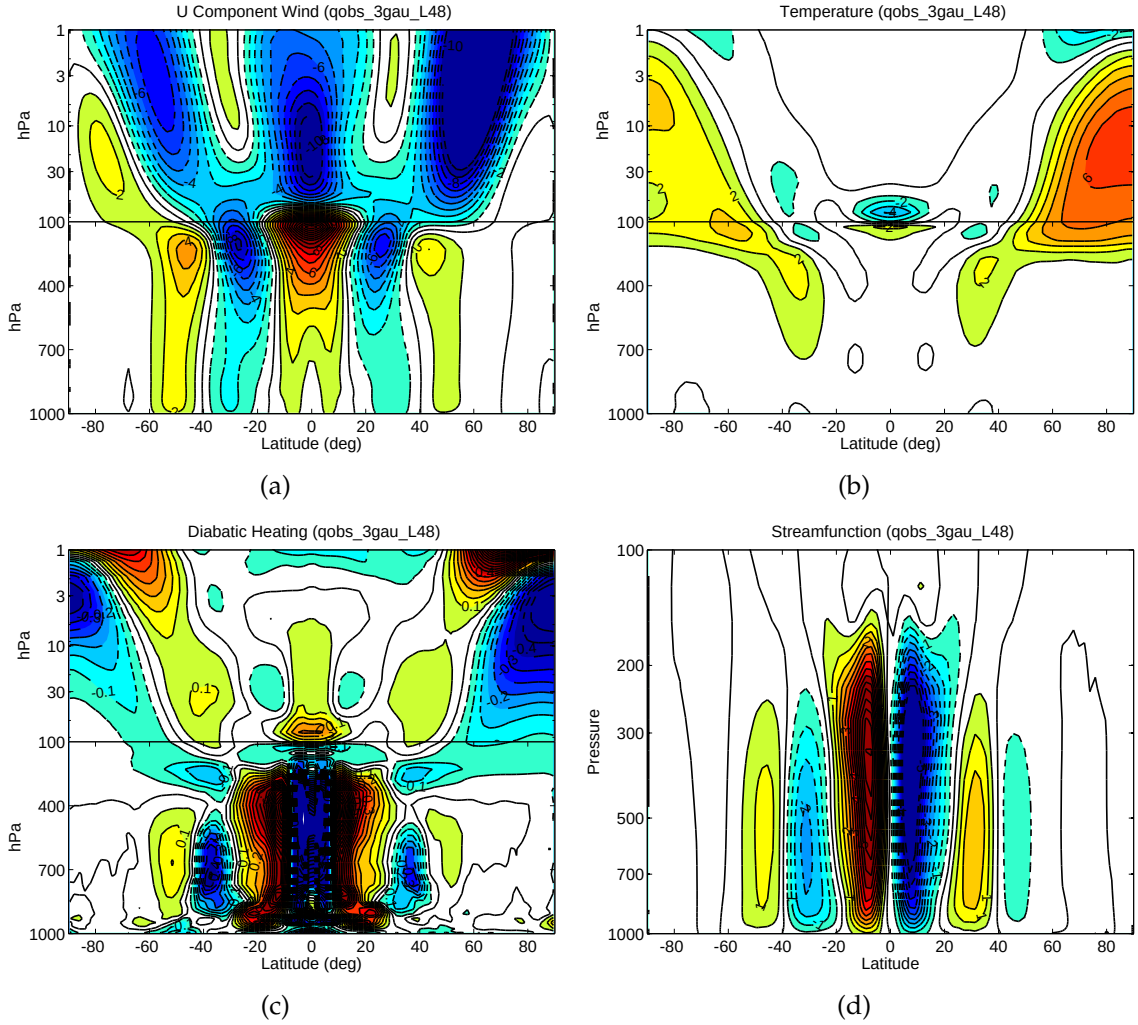

Figure 3.1: Anomaly fields of important meteorological properties derived from *Qobs_3gau*: (a) zonal mean zonal wind (units: m/sec, interval: 1 m/sec); (b) zonal mean temperature (units: K, interval: 1 K); (c) zonal mean diabatic heating (units: 10^5 K/sec, interval: $5{\times}10^3$ K/sec); (d) zonal mean streamfunction in the troposphere (units: 10^9 kg sec^{-1}, interval: 0.5×10^9 kg sec^{-1}), red for anticyclonic overturning while blue for cyclonic overturning.

tudes and cools down the ambient air in the stratosphere. Associated with the increased upwelling is an intensified adiabatic cooling. In order to compensate this adiabatic cooling and reach an ultimate energy balance, the in situ atmosphere requires more diabatic heating. Another interesting phenomenon about the residual circulation plot is that two ridges can be observed on this meridional plane in both hemispheres: one is at around 10° and the other is in the range of $50^\circ - 60^\circ$ with a slightly poleward skew. This denotes a spatial preference over specific region through BDC strengthening.

Besides BDC, the isentropic eddy mixing also is effected by the equatorial SST perturbation. Figure 3.3 illustrates the climatology (cf. Figure 3.3(a)) and changes (cf. Figure 3.3(b)) of the isentropic eddy mixing after the SST perturbation is imposed. The climatological isentropic eddy mixing peaks at polar tropopause and weakens in tropical stratosphere, subpolar stratosphere and subtropical troposphere. The weakening regions, with small equivalent length ratio $\tilde{\kappa}_{eff}$, coincide with the existence of tropical easterly flows in the stratosphere, polar night jets around polar vortices and subtropical jets in the troposphere (cf. Figure 2.3(d)), which is qualitatively consistent with the results in Haynes and Shuckburgh (2000b). Once the equatorial SST has been perturbed, the isentropic mixing increases significantly at the equatorward flank of polar night jets in the stratosphere, where is adjacent to the poleward side of conventional 'surf zone'. Another noticeable strengthening of isentropic mixing occurs at subtropical upper troposphere, coinciding with the deceleration of westerlies on the equatorward flank of subtropical jet. The major decline of isentropic mixing is at tropical troposphere, where superrotation is established (cf. Figure 3.1(a)). The potential physical connection between isentropic eddy mixing and zonal flow will be further discussed in Section 4.2.

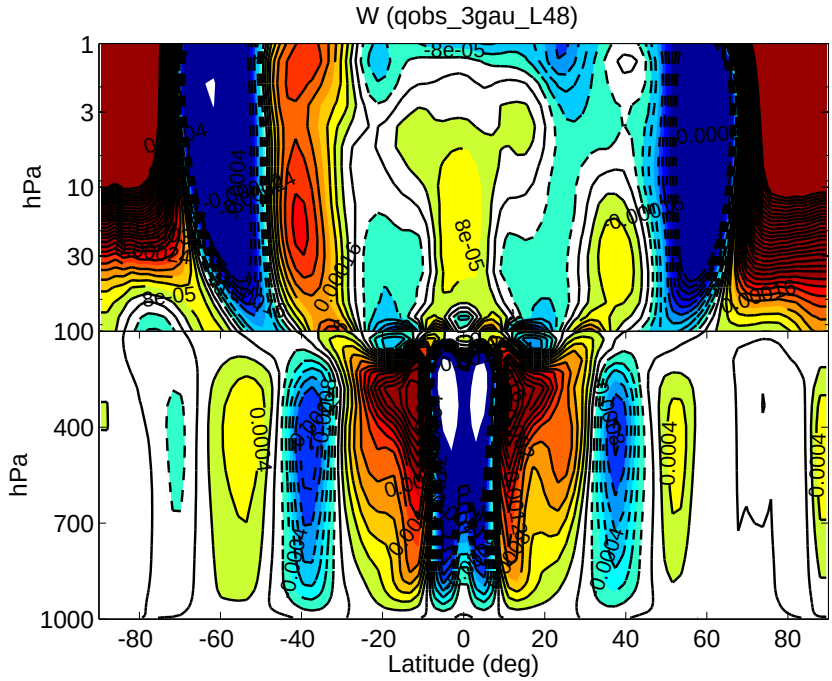

(a)

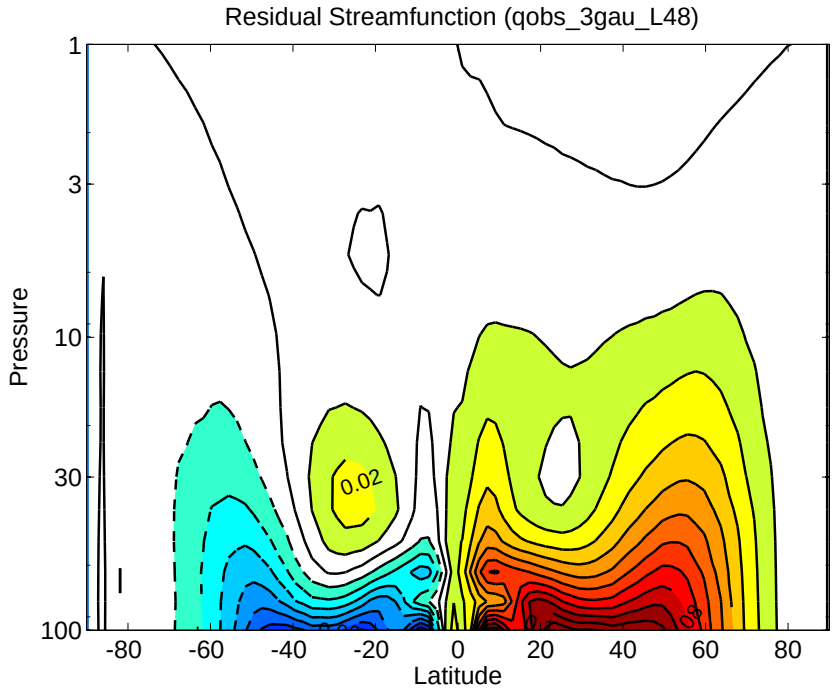

(b)

Figure 3.2: Anomaly fields in *Qobs_3gau* for: (a) conventional Eulerian mean vertical velocity $\bar{w}$ (units: m/sec, interval: 4×10^{-5}m/sec above 100 hPa, and 2×10^{-4}m/sec below 100 hPa); (b) stratospheric residual stream function (units: 10^9 kg sec^{-1}, interval: 0.01×10^9 kg sec^{-1}).

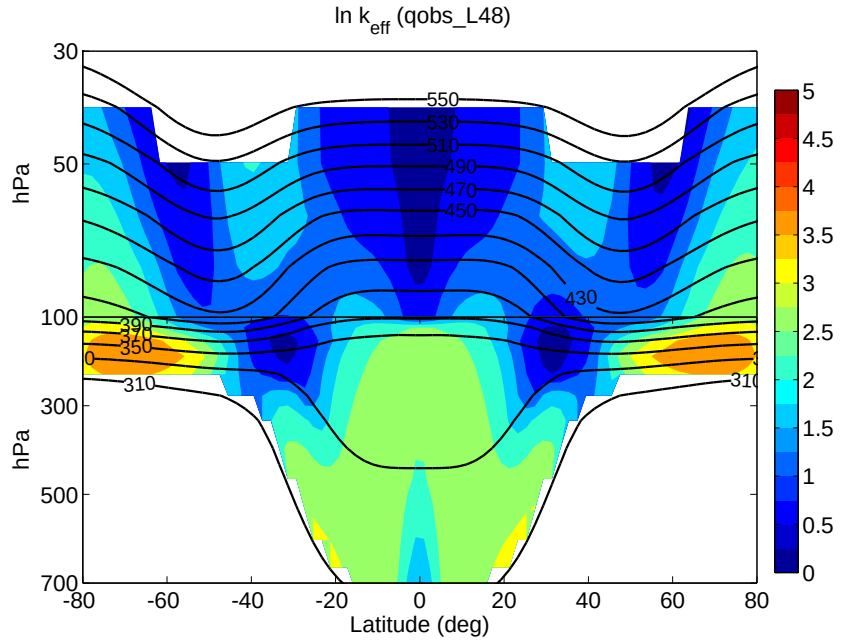

(a)

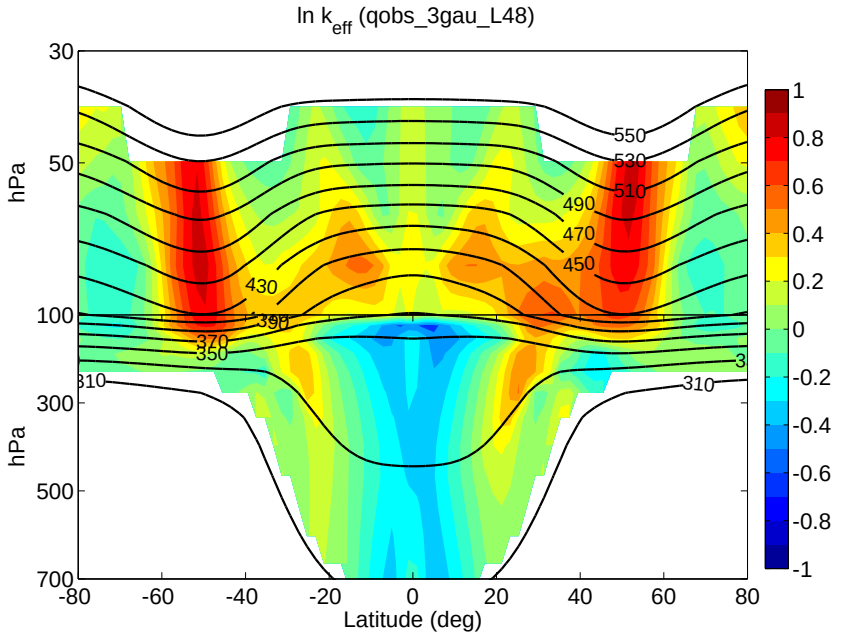

(b)

Figure 3.3: Logarithm of equivalent length ratio $\tilde{\kappa}_{eff}$ (colors) interpolated back into pressure coordinate and the interpolated isentropic surfaces (contours, units: K, interval: 20K): (a) total field in *Qobs*, which is a referenced climatology state; (b) anomaly field in *Qobs_3gau* when the equatorial Gaussian heating is added. During the interpolation, the climatology zonal mean temperature has been used.

Figure 3.4(a) illustrates the basic configuration of mass transport in the upper troposphere lower stratosphere (UTLS) region. The tropical troposphere, as well as almost anywhere below 250 hPa (dark blue region), mixes very quickly due to strong Hadley Cell, and synoptic turbulence in the troposphere. However, when it goes into the stratosphere, where diabatic circulation becomes relatively much weaker and synoptic eddy generation vanishes, the mass transport slows down massively with a significant increase of mean AOA. Moreover, the steep latitudinal gradients of the mean AOA found at $\pm 40^{\circ}$, $100 - 200\,\mathrm{hPa}$ (cf. Figure 3.4(c)), it spatially overlaps with the prevailing subtropical jets in the upper troposphere, which again demonstrates the blocking effects of strong zonal flow on mass transport. As both BDC and isentropic eddy mixing has been adjusted after perturbing the equatorial SST, the mass transport in the stratosphere, denoted by the mean AOA, tend to modify its structure as well. The mean AOA has been decreased in TTU region and even more largely inside the polar vortices, which is consistent with the overall strengthening of BDC (cf. Figure 3.2(b)), weakening of polar vortices (cf. Figure 3.1(b)), and intensified isentropic eddy mixing along the equatorward flanks of polar night jets (cf. Figure 3.3(b)). Thus, both BDC and isentropic eddy mixng here act coherently to weaken the transport barrier at stratospheric polar night jets (cf. Figure 3.4(d)) and reduce the mean AOA in the lower stratosphere (cf. Figure 3.4(b)). Note that the isentropic mixing does not always act positively in reducing mean AOA at any location, but current studies render some credits in supporting this argument over polar regions at lower stratosphere, which is consistent with current discussion here. Therefore, without specification, the following discussion in current study on the relationship between isentropic mixing and mean AOA is constrained within the high latitudes at lower stratosphere. Interesting changes

occur in the extratropical upper troposphere. The decelerated Hadley Cell is (cf. FIgure 3.1(d)) supposed to slow down the mass transport meridionally from tropics to mid-latitudes and consequently tends to increase the mean AOA on its poleward side, but, in fact, the mean AOA over these regions decreases with decreasing prick leaning along the poleward flanks of subtropical jets in both hemispheres ($40^\circ - 60^\circ$N/S, 100 – 200 hPa). This phenomenon highlights the potential crucial role of isentropic eddy mixing played in the mid-latitude upper troposphere overcoming the negative influences from the decelerated Hadley Cell and ultimately accelerating the mass transport in the extratropical upper troposphere by exciting air mass penetrating the subtropical jets — the conventional transport barriers.

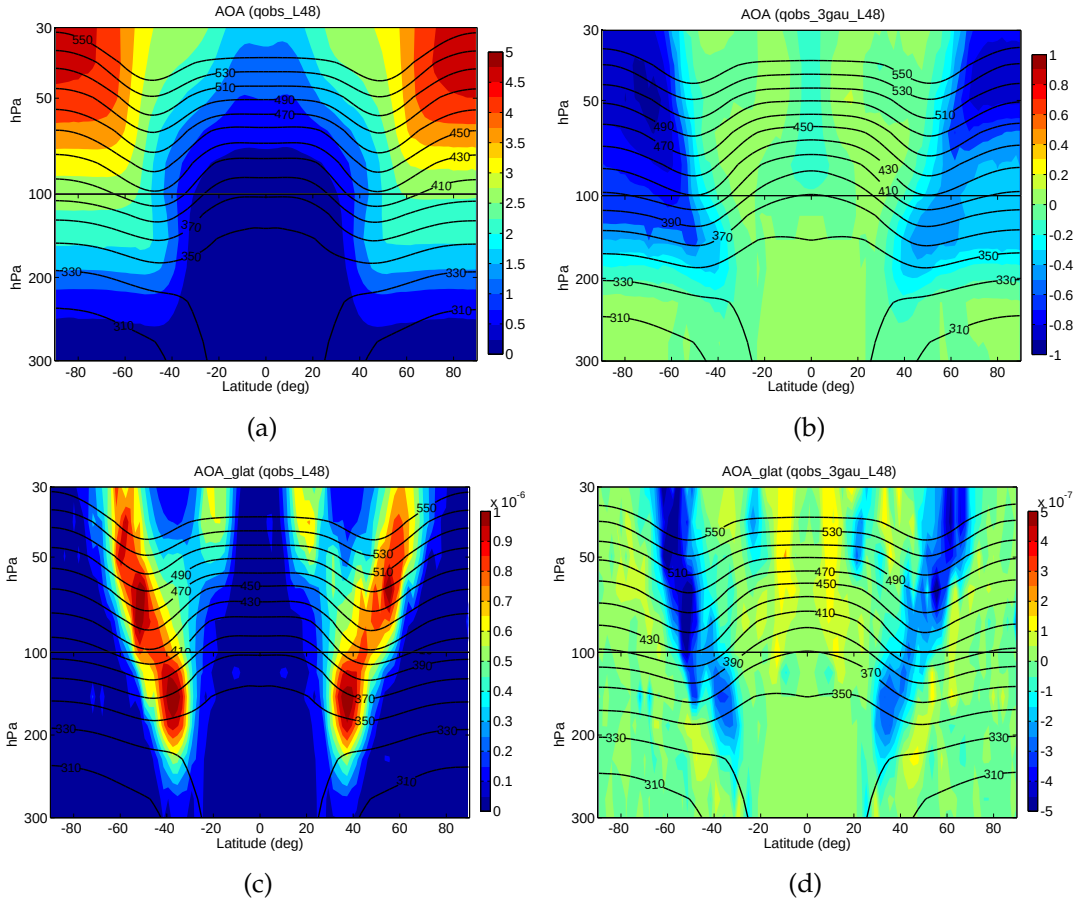

Figure 3.4: Similar to Figure 3.3, only the colors here denoting the mean AOA (units: year) of the clock tracer in (a)(b) whereas the latitudinal gradient of the mean AOA (units: year/m) in (c)(d), and the bottom plotting boundary has been set as 300 hPa to highlight the changes in upper troposphere.

CHAPTER 4

DYNAMIC DRIVERS

Chapter 3 has shown, the mass transport accelerates in UTLS under an equatorial two-dimensional Gaussian SST perturbation with contribution from both a strengthened BDC and intensified isentropic eddy mixing. In this chapter, we further explore the beneath dynamic drivers, which are responsible for the strengthened BDC, isentropic mixing and, of course, the accelerated mass transport in the stratosphere.

4.1 Drivers of Upwelling

BDC, the stratospheric diabatic circulation, is generally one cell hemispherically (cf. Figure 2.3(f)). Therefore, its strength, as well as changes of the strength, will be coherently represented by the tropical ascends (TTU), meridional flows and polar decends (cf. Figure 3.2). By following most of previous literatures, we choose the TTU to identify the strength of BDC as well. Multiple diagnostic methods are applied to unveil the physical drivers of strengthening TTU in frameworks of both zonal mean sense and full three-dimensional domain sense.

4.1.1 Zonal Mean

Unlike troposphere, the stratosphere is well stratified and so lacks of thermal factors to actively trigger the upwelling. Thus, the TTU must be dynamically driven by some mechanic torques as noted in Chapter 1. The TEM theorem, as well as a more developed 'downward control' principle, provides an effective

tool to verify these mechanic torques.

One major merit about using TEM theorem instead of the conventional Eulerian mean system is that the EP flux divergence (**DF**) in Equation 2.7a has been shown possessing clear physical linkage to eddies. In wave packets with steady, linear, conservative and quasi-geostrophic (QG) flow limits, the EP flux divergence will be identical to zero. In other words, the magnitude of EP flux divergence is nonzero if any unsteady, nonlinear, non-conservative or not quasi-geostrophic flow generated eddy is involved, which is quite common in nature. Then, embedded within the nonzero EP flux divergence, the eddies will exert their dynamic influences on the zonal mean flow through the TEM momentum balance. For instance, a region with negative value of **DF** (EP flux convergence) denotes where eddies converge, dissipate, and, by Equation 2.7a, induce poleward residual meridional motions — northward residual flow $\bar{v}^*$ in the Northern Hemisphere (NH) where the modified Coriolis parameter $\hat{f}$ is generally positive and southward residual flow in the Southern Hemisphere (SH) where the sign of $\hat{f}$ mostly flips to negative.

The theorem is clearly confirmed in the model by comparing Figure 4.1(a) with Figure 4.2. After anomalous Gaussian SST heating is imposed centered at the equator (*Qobs_3gau*), the anomaly field of EP flux divergence in the stratosphere shows a large domain of convergence for wave dissipation. As expected, overlapping the zone of anomalous EP flux convergence, corresponding anomalous poleward residual meridional flows $\bar{v}^*$ are found in both hemispheres indicating an intensification of BDC and the spatial pattern of $\bar{v}^*$ is highly consistent with the one of EP flux divergence. Look further closely into the deep tropics, though there are many spatially small scale perturbations below approxi-

mately 70 hPa, the patterns of both EP flux divergence and residual meridional velocity right above 70 hPa become gradually coherent and clear. The weakly anomalous EP flux convergence (wave dissipation) induces anomalous poleward meridional flows and further results in an anomalous mass divergence in the equatorial region. In order to reach the continuity balance (Equation 2.7b), a corresponding change on vertical motion is required. Mathematically speaking, both strengthened upwelling and downwelling could result in an anomalous divergence here, but as mentioned in Chapter 3, the anomalous divergence occurred in current *Qobs_3gau* simulation is balanced by the strengthening of TTU as many other models projected.

Further, the downward control principle, Equation 2.10 noted in Section 2.2.2, offers a quantitative approach in estimating how much of the variation of TTU is dynamically driven by eddies. Also, by recalculating residual vertical velocity using Equation 2.11, how much the anomaly in TTU is consistent with diabatic heating adjustment can be interpreted through the thermodynamic balance. The results are shown in Figure 4.3. Along the meridional cut at 70hPa (70hPa is chosen here since the height at this level is guaranteed to be in the stratosphere but not too distant away from the tropopause, which can represent the state of TTU in a good quality), strengthened TTU can be clearly distinguished in deep tropics, along with anomalous downward residual vertical motions dominating the region poleward of 60° in both hemispheres. Again, the spatial pattern of anomalies in residual vertical velocity $\bar{w}^*$ confirms the coherent strengthening of BDC noted in Chapter 3. Two anomalous secondary upwellings, weaker in magnitude, are discernible in the middle latitudes with their peaks centered close to 40° in each hemisphere. This is consistent with the residual streamfunction mapping in Figure 3.2(b), again ascertains the spatial prefer-

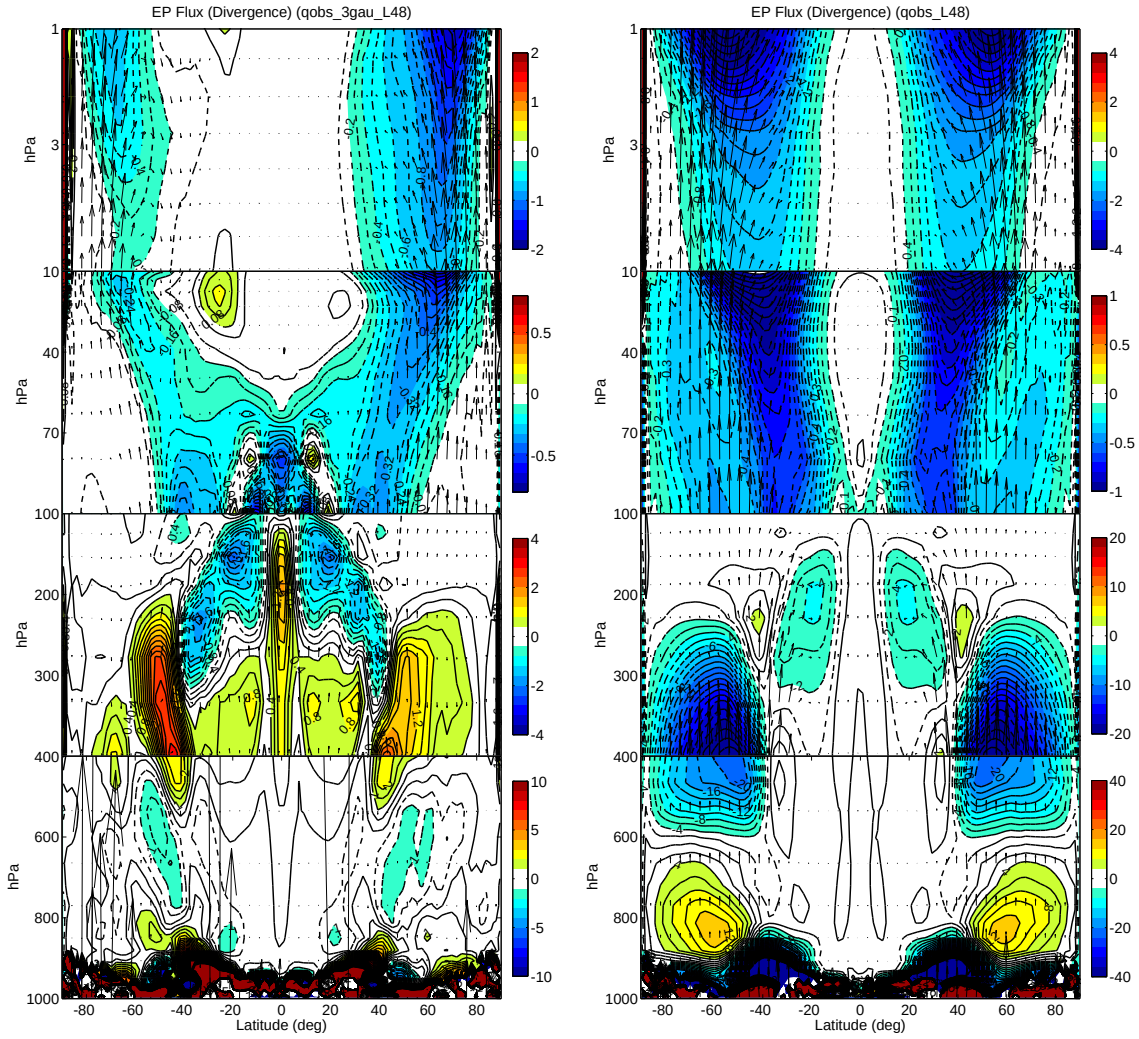

(a) (b)

Figure 4.1: Eliassen-Palm (EP) flux (vectors) and associated divergence **DF** (colors and contours), with red as the divergence zone for wave generation and blue as the convergence zone for wave dissipation: (a) anomaly field in *Qobs_3gau* (unit: $\mathrm{m\,sec^{-1}day^{-1}}$, interval: $0.1\,\mathrm{m\,sec^{-1}day^{-1}}$ (1-10 hPa), $0.04\,\mathrm{m\,sec^{-1}day^{-1}}$ (10-100 hPa), $0.2\,\mathrm{m\,sec^{-1}day^{-1}}$ (100-400 hPa), $0.5\,\mathrm{m\,sec^{-1}day^{-1}}$ (400-1000 hPa)) ; (b) total field in *Qobs* (unit: $\mathrm{m\,sec^{-1}day^{-1}}$, interval: $0.2\,\mathrm{m\,sec^{-1}day^{-1}}$ (1-10 hPa), $0.05\,\mathrm{m\,sec^{-1}day^{-1}}$ (10-100 hPa), $1\,\mathrm{m\,sec^{-1}day^{-1}}$ (100-400 hPa), $2\,\mathrm{m\,sec^{-1}day^{-1}}$ (400-1000 hPa)).

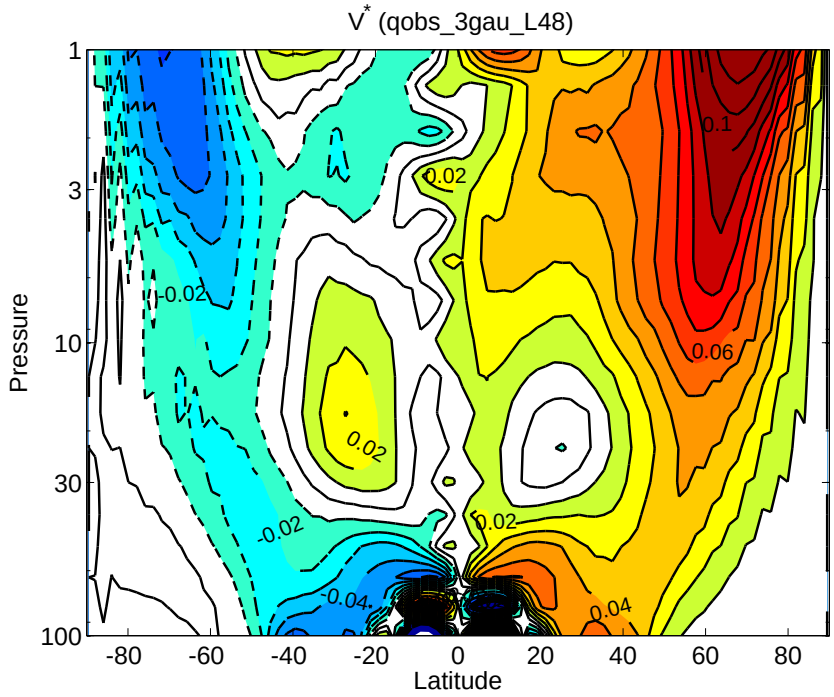

Figure 4.2: Anomaly field of residual meridional velocity v^* in the stratosphere in *Qobs_3gau* (units: m/sec, interval: 0.01 m/sec).

ence on BDC strengthening, which is probably related to a massive increase of wave breaking in extratropical stratosphere (cf. Figure 4.1(a)). In addition, the satisfactory agreement of three curves of the residual vertical velocity, derived from definition (solid), dynamic balance (dashed) and thermodynamic balance (dot-dashed) respectively, strongly certify current variation of TTU in the model is essentially driven by anomalous eddy forcing originated from the equatorial SST perturbation, and it is also coherent with the passive diabatic heating adjustment. Note that Φ_1 and Φ_2 are selected to be 15°S (-15°) and 15°N over deep tropical region here in the process of using Equation 2.10 to skip fatally small-Coriolis-parameter effect for guaranteeing computation stability within downward control analysis. Thus, the dynamic balance deduced residual vertical velocity in equatorial region, shown as the flat line, can be regarded as an

estimate of vertical velocity meridionally averaged over the range from 15°S to 15°N. Outside deep tropics, the original meridional interval set in the model is kept for optimal resolution. Moreover, the coherence of dynamic and thermodynamic balances is not constrained along the meridional cut. In a vertical view of the residual vertical velocity averaged over deep tropics (±15°), sustainably strengthened upwelling can be detected through the whole column of stratosphere (above 100 hPa), and all three evaluations of residual vertical velocity anomalies gives a good agreement among each other above 70 hPa. A local maximum of residual vertical velocity change can be found, though differs in magnitude by different approaches of estimation, right above the tropopause and decays smoothly as altitude increases until reaching 40 hPa, which resembles the results of Calvo et al. (2010) using advanced WACCM model to study the TTU behavior during warm ENSO events. The departure of thermodynamic-balance deduced residual vertical velocity ($\bar{w}^*_Q$) from the definition-derived one below 70 hPa might due to the omission of the vertical diffusion process in the model while diagnosing, and the reasons for the underestimate of residual vertical velocity by downward control analysis around 100 hPa and overestimates above 10 hPa remain unknown. However, these levels are either too high into the middle and upper stratosphere or too lower into the troposphere, within which does not interfere with the discussion on TTU in current study. Moreover, note from Figure 3.2(a), the meridional average range in Figure 4.3(b) is broader than what TTU truly occupies. Thus, the anomalous downwelling motions in the subtropics might contaminate the diagnostic results through averaging and the changes of TTU is consequently expected to be even more rigorous.

After knowing the current TTU changes is a dynamical consequence of eddy forcing in the stratosphere, the next question is where all these eddies come

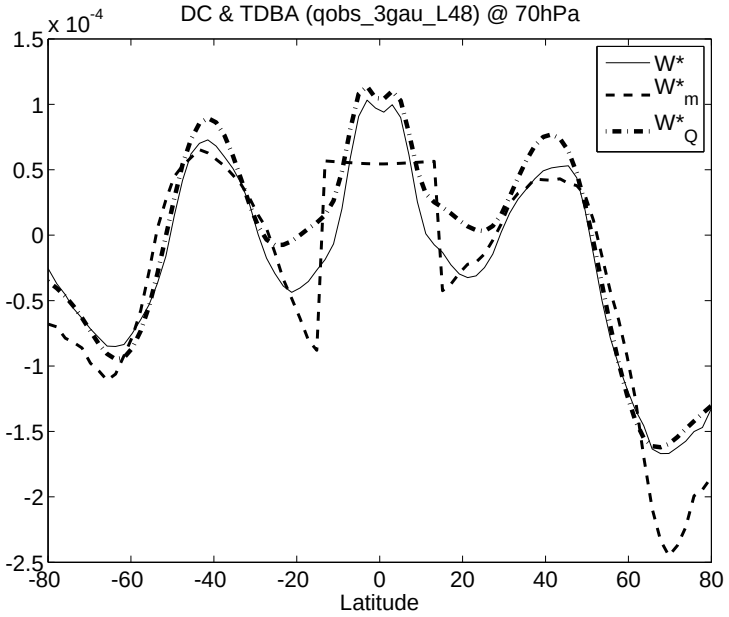

(a)

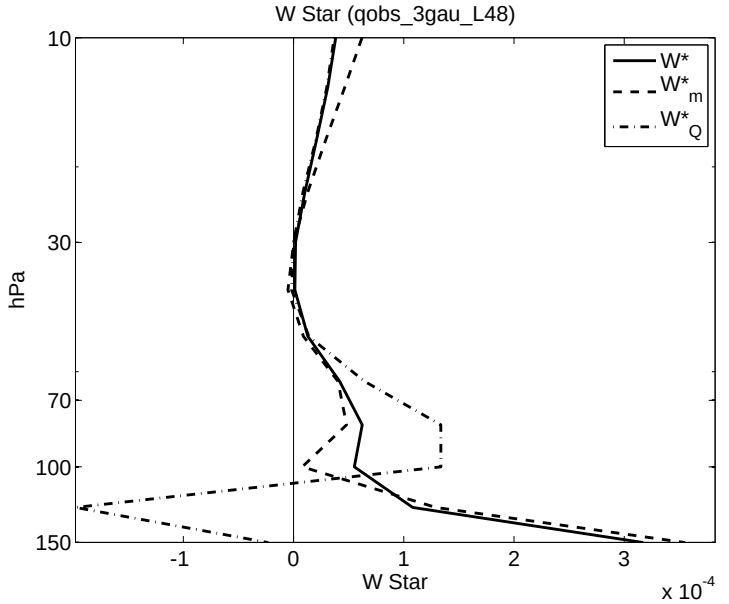

(b)

Figure 4.3: Dynamic and thermodynamic balance of variation of TTU in *Qobs_3gau*, the residual vertical velocity $\bar{w}^*$ (unit: m/sec) are plotted (a) along a meridional line at 70 hPa, and (b) in a vertical configuration and zonally averaged from 15°S to 15°N. The residual vertical velocities are obtained from three approaches of evaluation: direct definition $\bar{w}^*$ (solid line, see Equation 2.6b); dynamic balance $\bar{w}^*_m$ (dashed line, also known as downward control principle, see Equation 2.10); thermodynamic balance $\bar{w}^*_Q$ (dot-dashed line, see Equation 2.11).

from. Here, EP flux is analyzed with its divergence zone being regarded as the wave origin (Edmon Jr et al. 1980, Garny et al. 2011). From Figure 4.1(a), it is clear that the eddies, with which dissipate and drive the TTU in the stratosphere, are not generated locally since no significant in situ EP flux divergence zone are found. However, once enlarging the search mapping of EP flux divergence into the whole stratosphere and troposphere combined, a large domain of anomalous EP flux divergence is discernible aligning over (sub)tropics in the middle troposphere (300 hPa - 500 hPa), and extends almost symmetrically departing from the equator with an erected intrusion into a height close to 100 hPa in deep tropics (±10°). Two more EP flux divergence anomaly zones are found in the middle latitudes, associating with the relatively weak EP flux convergence zones right below, which oppositely mirror the configuration of total field of EP flux divergence in *Qobs* shown in Figure 4.1(b). Therefore, it is suspected that, due to the equatorial SST increase, less eddies are generated in extratropical region. However, synchronizing with a much stronger suppression on eddy dissipation, surprisingly more eddies are able to penetrate the tropopause and contribute to drive the BDC in the stratosphere. Further, as the wave eddies are generated remotely in the troposphere, what factors are affecting their vertical propagation into the stratosphere? In order to find the answers for all these questions, the EP flux divergence field has been decomposed into stationary eddy and transient eddy following Equation 4.1, which is essentially the scheme utilized in Holton (2004).

$$\bar{u} = [\bar{u}] + \bar{u}^* \tag{4.1a}$$

$$\bar{\theta} = \left[\bar{\theta}\right] + \bar{\theta}^* \tag{4.1b}$$

$$\overline{v'u'} = \left[\overline{v'u'}\right] + \overline{v'u'}^* \tag{4.1c}$$

$$\overline{v'\theta'} = \left[\overline{v'\theta'}\right] + \overline{v'\theta'}^{*} \tag{4.1d}$$

$$\overline{\omega'u'} = \left[\overline{\omega'u'}\right] + \overline{\omega'u'}^{*} \tag{4.1e}$$

$$\mathbf{DF}\left(\bar{u}, \bar{\theta}, \overline{v'u'}, \overline{v'\theta'}, \overline{\omega'u'}\right) = \mathbf{DF}\left([\bar{u}], \left[\bar{\theta}\right], \left[\overline{v'u'}\right], \left[\overline{v'\theta'}\right], \left[\overline{\omega'u'}\right]\right) + \text{residue} \tag{4.1f}$$

Similar to the overbar noted in Equation 2.5, square brackets here denote temporal average, and unlike what used in the definition of residual velocities, star marks here indicate the departure from its temporal mean. Therefore, the EP flux divergences (**DF**) recalculated based on the temporal averaged properties are termed as the stationary component, and the residue after subtracting the stationary component from the original total EP flux divergence are termed as the transient component.

Given the decomposition, it is proven that, in terms of anomaly field, the transient eddies prevail in extratropics and stationary eddies are more important in (sub)tropical regions (cf. Figure 4.4). It is reasonable since the spatially fixed SST perturbation is mainly situated in tropics and synoptic events occur in extratropics with higher frequency. As stationary eddies dominate in the tropics where TTU spatially overlaps, elucidating the interferences of stationary wave component upon TTU variation is absolutely important. In Figure 4.5, the total field of stationary eddies associated EP flux divergence (**DF**) and zonal mean zonal wind ($\bar{u}$) in *Qobs_3gau* are depicted to interpret stationary wave generation and propagation process. Marked as those EP flux divergence zone, most of the stationary waves are generated in deep tropics. As to propagation, following Charney-Drazin criterion (Charney and Drazin 1961), the background zonal wind threshold for vertical propagation of eddies is shown as Equation 4.2.

$$0 < \bar{u} - c_p < U_C \tag{4.2}$$

Here, c_p is the phase speed of eddies and, for stationary waves, it equals to zero. U_C is the critical velocity determined by wavelength of eddies, geographic locus and ambient atmospheric stability. As a result, only eastward winds, but not overly strong, can allow the stationary eddies to propagate vertically, penetrate from troposphere into stratosphere, and ultimately to strengthen the BDC. Though not commonly seen in reality, the superrotation in the UTLS making the zonal mean zonal wind here slightly westerly, which indeed favors the vertical propagation of stationary eddies. However, the eddies initiate to dissipate (EP flux turns to convergent) in the upper troposphere right below 100 hPa where is still far away from the zero wind line in the stratosphere. This might be due to the local maximum of zonal flows at 100 - 150 hPa suggesting the sensitivity of eddy vertical propagation upon upper threshold U_C. Overlap between large subtropical dissipation zones in the upper troposphere and subtropical jets boundary also certify the blocking effects from zonal flow exceeding a speed of U_C. As background zonal winds gradually turn into easterlies, stationary eddies persist to dissipate in the stratosphere above 70 hPa, and dynamically exert mechanic torque exciting poleward meridional motions in the process of reinforcement of the TTU.

4.1.2 Zonal Asymmetry

Embedded within the Gaussian SST perturbation in *Qobs_3gau*, zonal asymmetry of the forcing tends to make atmospheric responses not uniformly dis-

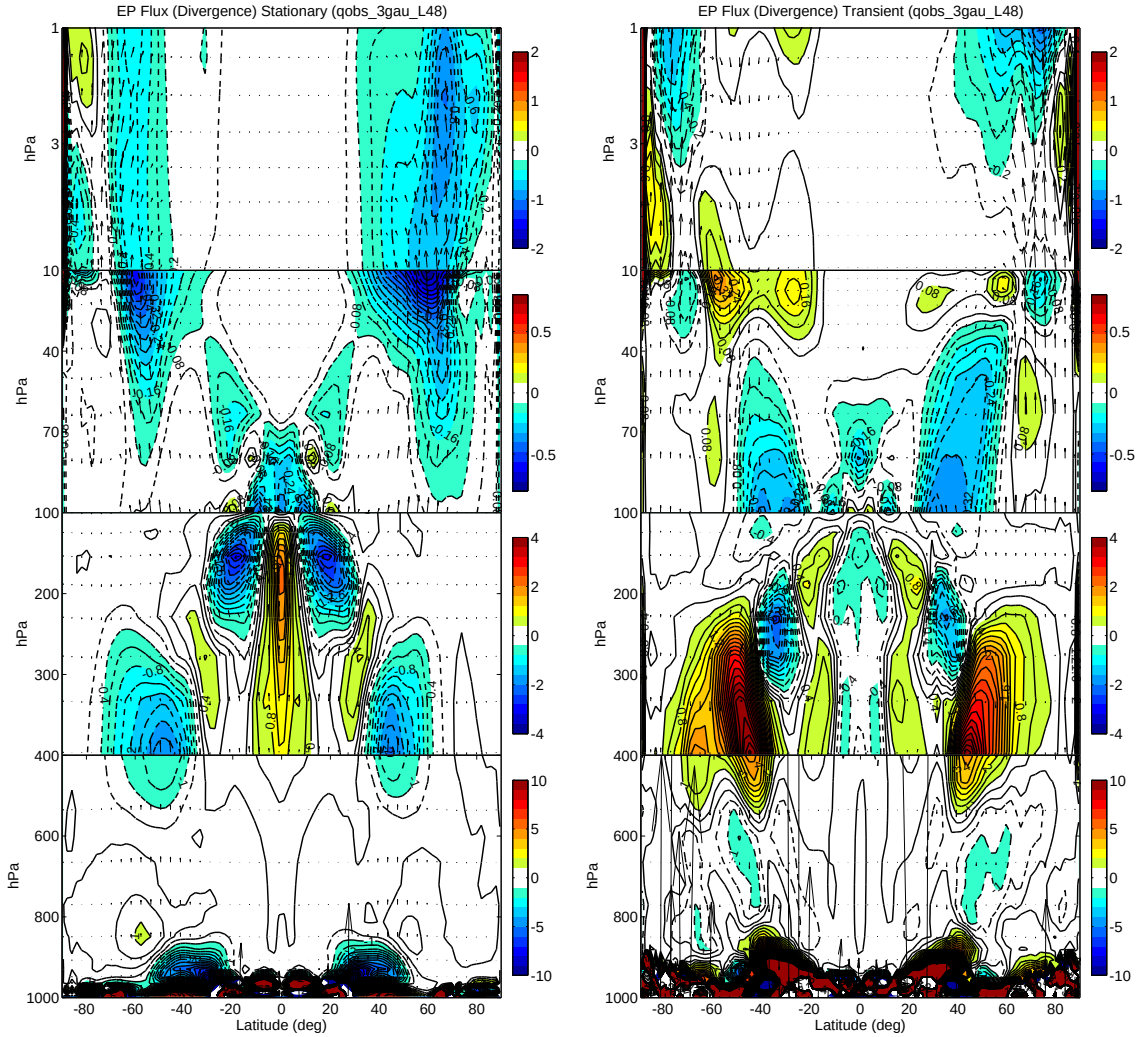

Figure 4.4: Temporal decomposition of anomalous EP flux and its divergence **DF** (unit: $\mathrm{m\,sec^{-1}day^{-1}}$) in *Qobs_3gau* (a) stationary component; (b) transient component. (interval: $0.1\,\mathrm{m\,sec^{-1}day^{-1}}$ (1-10 hPa), $0.04\,\mathrm{m\,sec^{-1}day^{-1}}$ (10-100 hPa), $0.2\,\mathrm{m\,sec^{-1}day^{-1}}$ (100-400 hPa), $0.5\,\mathrm{m\,sec^{-1}day^{-1}}$ (400-1000 hPa))

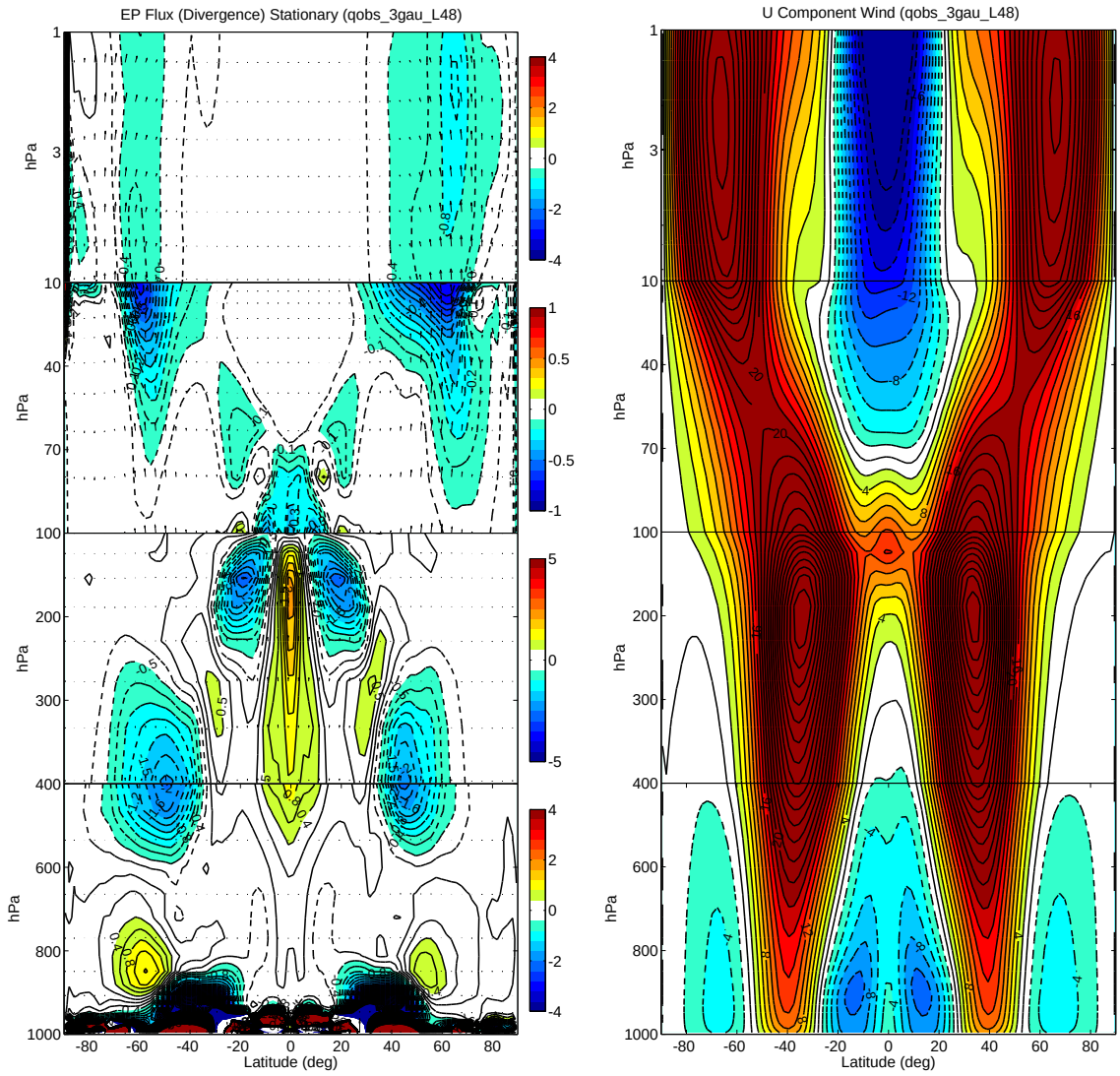

Figure 4.5: Stationary waves propagation in *Qobs_3gau*: (a) total field of stationary EP flux (vectors) and its divergence **DF** (shadings and contours, units: $\mathrm{m\,sec^{-1}day^{-1}}$, interval: $0.2\,\mathrm{m\,sec^{-1}day^{-1}}$ (1-10 hPa), $0.05\,\mathrm{m\,sec^{-1}day^{-1}}$ (10-100 hPa), $0.25\,\mathrm{m\,sec^{-1}day^{-1}}$ (100-400 hPa), $0.2\,\mathrm{m\,sec^{-1}day^{-1}}$ (400-1000 hPa)); (b) total field of zonal mean zonal wind (units: m/sec, interval: 2 m/sec).

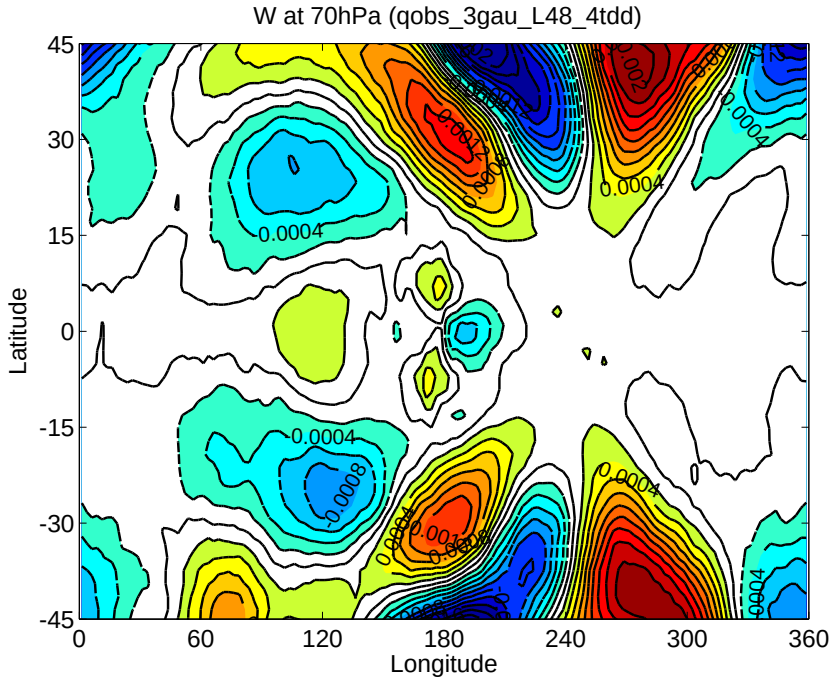

Figure 4.6: Vertical velocity w anomalies in *Qobs_3gau* (unit: m/sec, interval: 2×10^{-4} m/sec) on a latitudinal-longitudinal cross section plane at 70 hPa.

tributed along the equator. As illustrated in Figure 4.6, the anomaly of vertical velocity at 70 hPa in the deep tropical region, though relatively weaker in magnitude comparing the one in subtropics, clearly bears latitudinal oscillation right above the SST heating source at 180°, with two off-equator strengthening centers on the westward side of surface heating center and one weakening center centered at the equator on the eastward side of surface heating center. What factors result in such zonal asymmetric responsive pattern of TTU? Are they still wave driven as what have been shown in the two-dimensional zonal mean analysis?

Figure 4.7 clearly marks the trace of tropical waves involved in *Qobs_3gau*. In Figure 4.7(a), two negative peaks of temperature anomalies centered longitudinally at 180° and latitudinally at approximately 20° in both hemisphere are

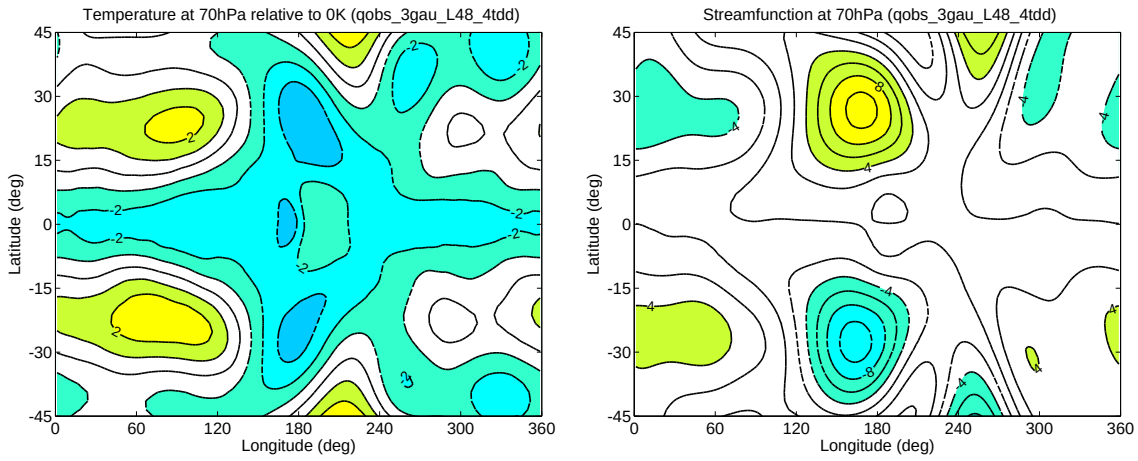

(a) (b)

Figure 4.7: Tropical wave pattern in *Qobs_3gau* at 70 hPa: (a) Temperature anomalies (unit: K, interval: 1 K); (b) horizontal stream function ψ anomalies (unit: $m^2\ sec^{-2}$, interval: $2\ m^2\ sec^{-2}$) with zonal mean removed.

observed representing the persistent existence of suspicious Rossby waves. In the meanwhile, a long tail of negative temperature anomalies circling the equatorial loop indicates a steady presence of tropical Kelvin wave. Combining them together, the wedge-shaped temperature anomalies at 70 hPa over tropical region geographically display a reminiscence of Matsuno-Gill pattern (Matsuno 1966, Gill 1980), which generally thought to be forced by surface oceanic heating. The only significant difference is the flip of sign in temperature anomaly field, probably since we are discussing it in the stratosphere. In addition, with zonal mean component removed, the adjusted horizontal stream function ψ (cf. Figure 4.7(b)) displays significant zonal asymmetry in subtropics with strongest perturbation situated almost identically at the negative peaks of temperature anomalies. The behaviors of both fields suggest strong wave activities, linked to the equatorial SST heating imposed, are occurring at (sub)tropics in current experiment *Qobs_3gau*, inherently with large zonal asymmetry.

Analogous to the downward control applied in the zonal mean analysis through Section 4.1.1, vorticity balance, a transformed form of momentum balance, has been utilized in this subsection to detect the dynamic factors behind the zonal asymmetric responses of atmosphere, particularly the TTU. Details about vorticity balance analysis can be found in Section 2.2.3. In a climatology limit, the vorticity tendency $\partial\zeta_a/\partial t$ is negligible. Following Equation 2.12, the anomalies of the rest three terms on the left hand side in experiment *Qobs_3gau* are calculated and depicted in sequence in Figure 4.8. Overall speaking, the absolute vorticity advection by non-divergent winds $-\mathbf{V}_\psi \bullet \nabla\zeta_a$ and the production of absolute vorticity and horizotal divergence $\zeta_a\nabla \bullet \mathbf{V}$ dominate in the vorticity balance in most (sub)tropical regions. However, as illustrated in Figure 4.8(d), for deep tropics ($< \pm 15°$) longitudinally averaged from 160° to 180° where the cores of positive vertical velocity anomaly are located, the absolute vorticity advection by divergent winds $-\mathbf{V}_\chi \bullet \nabla\zeta_a$ starts to act as importantly as the production term $\zeta_a\nabla \bullet \mathbf{V}$ in compensating the effects of absolute vorticity advection by non-divergent winds $-\mathbf{V}_\psi \bullet \nabla\zeta_a$. For absolute vorticity advection by non-divergent winds specifically, it inherently relates to the eddies (represented through horizontal stream function $\psi = \psi_0 \exp\left(ik_x x + ik_y y + ik_z z - i\omega t\right)$) in Equation 4.3.

$$-\mathbf{V}_\psi \bullet \nabla\zeta_a = -\left\{\hat{k} \times \nabla\psi\right\} \bullet \nabla\left\{\nabla^2\psi + f\right\} \tag{4.3}$$

Hence, once the equatorial SST is perturbed, intensified deep convection tends to robustly generate large packs of tropical eddies. These eddies further propagate vertically into the stratosphere and dissipate there resulting in the changes of absolute vorticity advection by non-divergent winds $-\mathbf{V}_\psi \bullet \nabla\zeta_a$

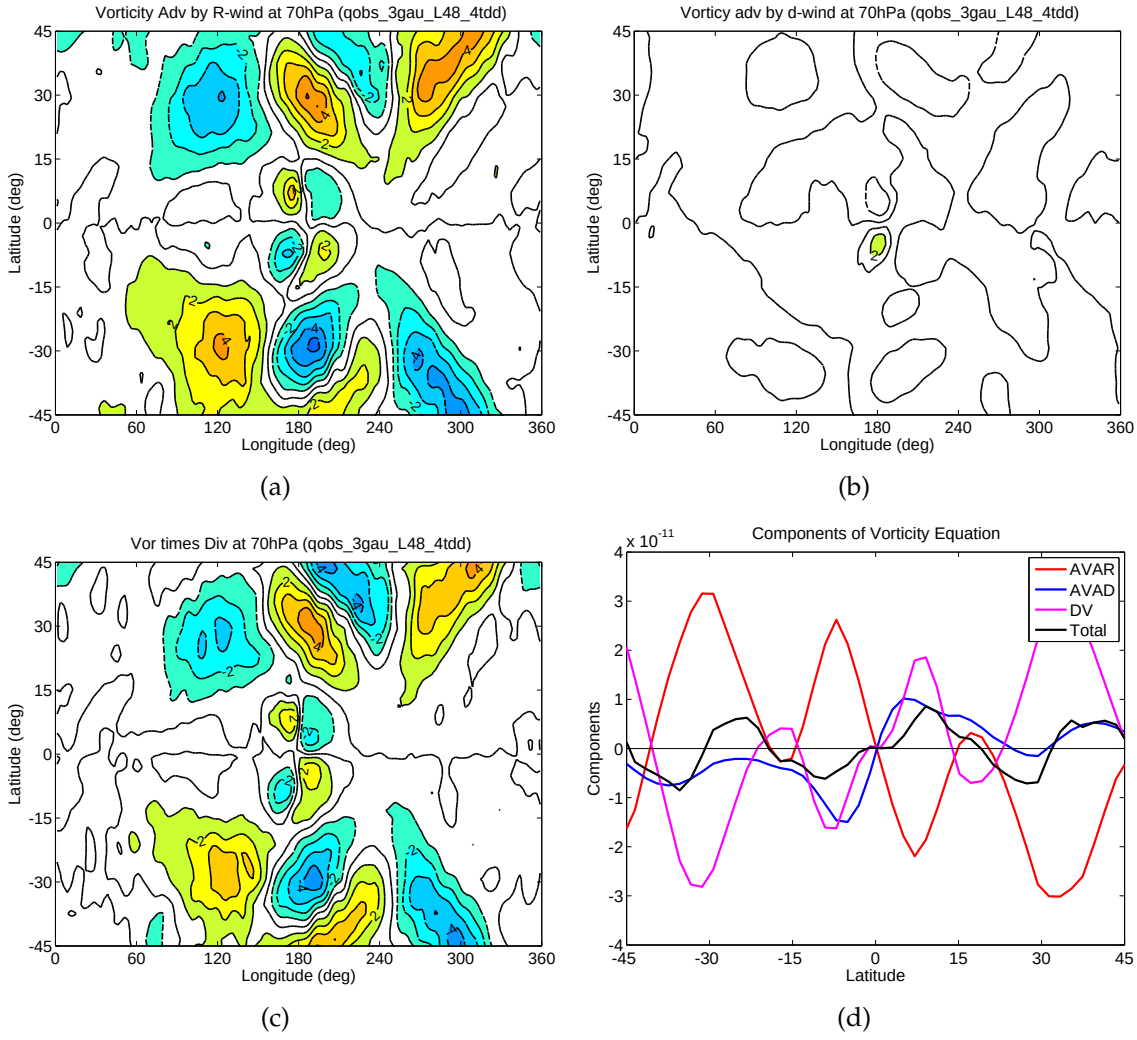

Figure 4.8: Vorticity balance in *Qobs_3gau* at 70 hPa plotted in terms of anomaly fields: (a) absolute vorticity advection by non-divergent winds ($-\mathbf{V}_\psi \bullet \nabla\zeta_a$); (b) absolute vorticity advection by divergent winds ($-\mathbf{V}_\chi \bullet \nabla\zeta_a$); (c) production of absolute vorticity and divergence ($\zeta_a\nabla \bullet \mathbf{V}$); (d) all terms in vorticity balance as well as their sum averaged over 150°-200° where strongest SST perturbation situated (AVAR: $\mathbf{V}_\psi \bullet \nabla\zeta_a$, AVAD: $\mathbf{V}_\chi \bullet \nabla\zeta_a$, DV: $\zeta_a\nabla \bullet \mathbf{V}$). (unit: 10^{-11} m^2 sec^{-2})

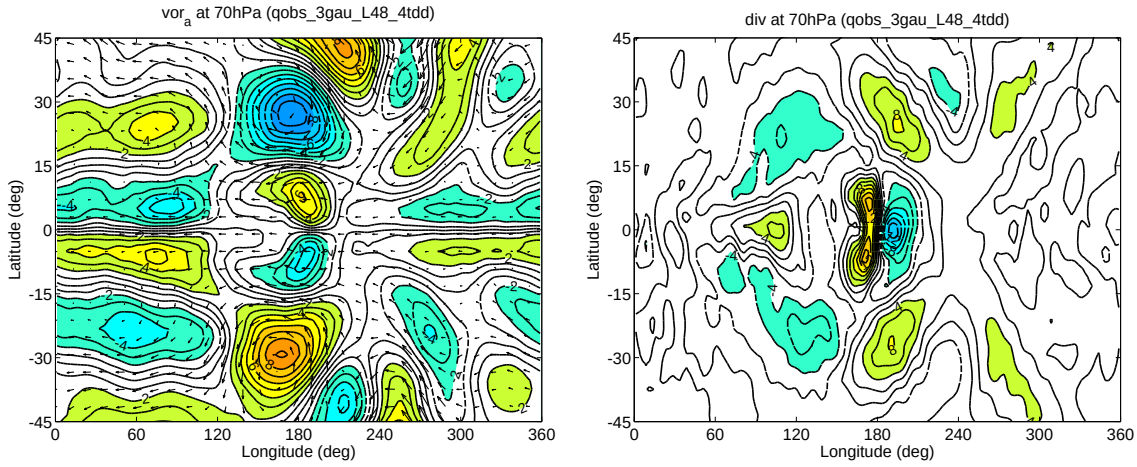

(a) (b)

Figure 4.9: Anomaly fields in *Qobs_3gau* at 70 hPa in terms of: (a) velocity (vectors) and absolute vorticity (shadings and contours, unit: $10^{-6}\,\mathrm{sec}^{-1}$, interval: $10^{-6}\,\mathrm{sec}^{-1}$); (b) divergence (unit: $10^{-7}\,\mathrm{sec}^{-1}$, interval: $2\times10^{-7}\,\mathrm{sec}^{-1}$)

at the level of interest. On the westward side of SST perturbation center, the wave induced changes of absolute vorticity advection by non-divergent winds $-\mathbf{V}_\psi \bullet \nabla\zeta_a$ are then balanced by the alteration of absolute vorticity advection by divergent winds $-\mathbf{V}_\chi \bullet \nabla\zeta_a$ and the production term $\zeta_a\nabla \bullet \mathbf{V}$, which are both strongly connects to spatial correspondence of vorticity and divergence fields shown in Figure 4.9. The anomalous divergence field then, specifically, triggers the strengthening of local upwellings, as well as downwelling, in deep tropics (comparing Figure 4.9(b) with Figure 4.6).

Simulation results from current study differ from Norton's work (Norton 2006) arguing the the absolute vorticity advection by non-divergent winds is mostly compensated by the the same quantity advected by divergent winds, but they used a different model, and their study implemented the analysis at 150 hPa, a layer still in the upper troposphere. Nevertheless, both studies qualitatively indicate that the inherent zonal asymmetry of eddies results in the zonal

asymmetry of TTU responses, which again emphasizes the anomaly of TTU is physically driven by eddies associated with the imposed SST heating, and it is in a good consistency of conclusion derived through two-dimensional dynamic analysis in Section 4.1.1.

4.2 Drivers of Isentropic Mixing

The intensity of isentropic mixing highly depends on the density of wave breaking (Haynes and Shuckburgh 2000a). Accompanying with sufficient wave breaking (i.e. eddy dissipation), tracer contours (here the EPV isopleths) stretch to provide room, as well as larger local concentration gradient, for mixing along isentropic surfaces. On the other hand, the zonal mean flow not only directly participates to determine the environment for mixing due to wave breaking, but also affects the propagation and dissipation of eddies, and further indirectly exerts its impact on isentropic mixing. Generally, speedy zonal flows suppress isentropic eddy mixing while calm zonal winds favor it. The mathematical description of relationship among wave breaking, zonal flow and isentropic eddy mixing is given by Yang et al. (1990) on isentropic levels (see their Equation 24). It confirms the critical roles of wave breaking (EP flux pseudodivergence) and zonal flow (embedded within the EPV) played in the determination of strength of isentropic mixing.

For climatology in the control run *Qobs*, regions with little isentropic mixing (cf. Figure 3.3(a)) are characterized with either weak wave breaking (cf. Figure 4.1(b)) or strong zonal winds (cf. Figure 2.3(d)), or both. It is ascertained by the anomaly field of isentropic eddy mixing in *Qobs_3gau* with equatorial heating

as well. Specifically, massive increases of isentropic eddy mixing appear within the stratospheric polar night jets ($40^\circ - 60^\circ$N/S, $50 - 100$ hPa), which spatially overlap with strongly increased local eddy dissipation (cf. Figure 4.1(a)) and decelerated westerlies (cf. Figure 3.1(a)). So is the similar case for the tropospheric increase of isentropic eddy mixing ($20^\circ - 30^\circ$N/S, $100 - 300$ hPa), simultaneously accompanying with slight increase of wave breaking and, more importantly, the weakening of subtropical jet streams. Eddy dissipation in tropical troposphere is complicated. On one hand, large amount of stationary eddies are generated in the vicinity of deep tropics, spatially very restrained, due to highly activated deep convection by equatorial SST perturbation. This means little wave breaking will occur over the region. On the other hand, eddy dissipation indeed increases over the climatological subtropical dissipation zones. Despite the spatial diversity of behaviors of eddy dissipation, thanks to the equatorial superrotation noted in Chapter 3 characterized with relatively strong westerlies, isentropic eddy mixing in tropical troposphere displays a consistent decrease.

CHAPTER 5

TRANSPORT SENSITIVITY TO CHANGES OF SST PERTURBATION

Previous chapters have shown how the stratospheric transport will vary in response of an equatorial SST perturbation, and how this variation behaves in terms of changes of BDC and changes of isentropic eddy mixing separately. Also, the fact that, current variation of stratospheric transport is dynamically associated with SST-forced eddies, has been reasoned. In this chapter, the scope of the study extends to the cases having SST perturbation centered at higher latitudes ϕ_0 or with broader (or narrower) longitudinal span λ_S. By searching for consistent behaviors under different types of perturbation, these sensitivity experiments assist us to discover the region in which BDC, as well as isentropic eddy mixing, tend to affect the transport most.

5.1 Heating Center Latitude ϕ_0

For experiments discussed in this section, the SST perturbations are still following a typical Gaussian distribution, with heating maximum I_G at 3K and longitudinal span $\lambda_S = 30°$. The difference is the location of heating center ϕ_0 (see Section 2.1). It is no longer lingered at the equator ($\phi_0 = 0$), but with a gradual northward shift (5° interval) until arriving at 30°N (cf. Figure 2.2(a)). Moreover, as heating center latitude ϕ_0 moving poleward, the spherical effect will squeeze the size of heating with an unchanged longitudinal span λ_S at higher latitudes, which means the total SST perturbation input into the model tends to decrease then. Since the heating center, source of forcing, departs away from the equator into subtropical region and its size changes, it will perturb the at-

mosphere very differently in terms of zonal wind, temperature, diabatic heating, circulation and etc.. Adjustments on these meteorological fields will further inherently change the dynamic and thermodynamic backgrounds for eddy generation, propagation and dissipation, which will lead to different behaviors of both BDC and isentropic eddy mixing, and consequently a different structure of stratospheric mass transport.

As illustrated in Figure 5.1, after shifting heating center latitude ϕ_0 to 15°N, the SH, having less SST perturbation, tends to generate much weakened atmospheric responses in an absence of forcing. As to the NH, bearing the majority of SST perturbation but with a reduced global amount, responds similarly to the one *Qobs_3gau* with equatorial heating. Nevertheless, there are still two noticeable differences brought by this off-equator heating: (a) stronger zonal wind anomaly in the tropospheric extratropical NH; (b) much more pronounced spatial preference for BDC intensification in NH, as two strengthening zones are clearly separated by a weakening zone centered at 20°N. When ϕ_0 moves further northward to 30°N, somewhere sufficiently distant from the deep tropical region, the atmosphere reacts in an utterly different way. Now the polar night jets in both hemispheres are turning stronger rather than in a suppressed phase in experiments with relatively near-equator heating. Due to the acceleration of polar night jets, the polar vortex in SH becomes colder than the climatology in *Qobs* and there is no warming sign for NH polar vortex either. Moreover, the lowermost portion of BDC starts to decelerate, which will result in a slower mass transport across isentropic surfaces in the lower stratosphere. It is odd to observe the atmospheric responses are stronger in SH while the forcing is imposed in NH. However, it is too early to say there is a remote interaction pattern embedded just based on one sensitivity experiment.

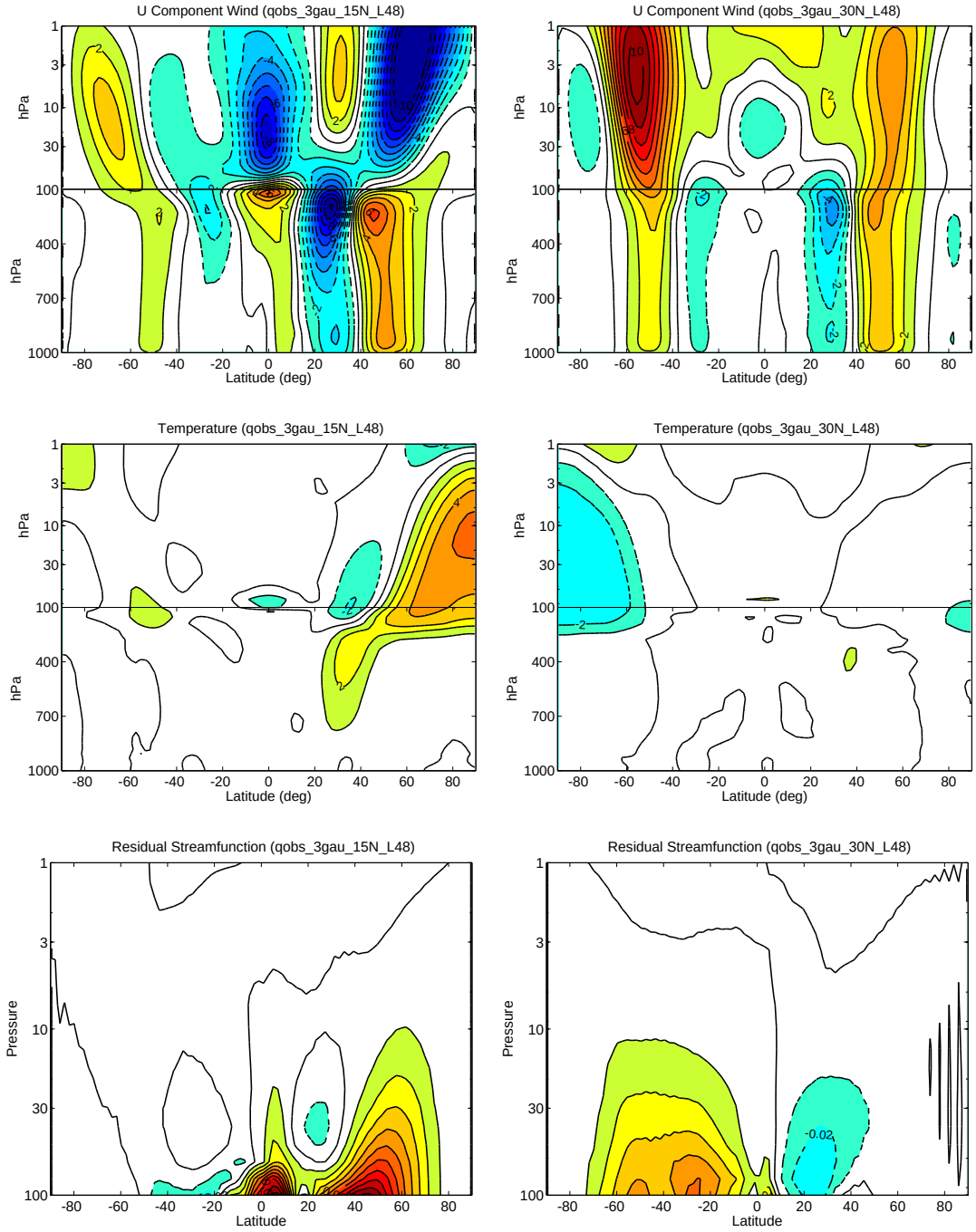

Figure 5.1: Anomaly fields of zonal mean zonal wind (first row), zonal mean temperature (second row) and stratospheric residual stream function (third row) for experiments (left column) *Qobs_3gau_15N*; and (right column) *Qobs_3gau_30N*. Units and intervals applied in all experiments here follow the settings noted in Chapter 3.

As we have seen, the shift of heating center latitude ϕ_0 can result in very different atmospheric responses, but what do these mean exactly to the stratospheric mass transport? Figure 5.2 provides some of the information that could help us establish a better understanding. 70 hPa and 100 hPa are chosen here as two reference levels to observe the transport changes in lower stratosphere and at tropopause respectively. As two crucial elements greatly influencing the stratospheric transport, the strength of BDC is indicated by the residual vertical velocity $\bar{w}^*$ and the extent of isentropic eddy mixing is indicated by the equivalent length ratio $\tilde{\kappa}_{eff}$. Finally, the mean AOA is adopted to assess the changes of transport speed. Following the northward shift of ϕ_0, both TTU and polar downwelling show a consistent decrease of strengthening and even turn into a phase of weakening once ϕ_0 exceeds some critical value pushing the heating center sufficiently away from the equator (cf. Figure 5.2(a)). Hence generally, the strengthening of BDC in the stratosphere becomes weaker if the heating center moves away from the equator. The isentropic eddy mixing bears a responses similar to the BDC. The northward shift of ϕ_0 reduces the excitement from the SST forcing to produce more isentropic eddy mixing, especially over the polar night jets region. Since both strengthening of BDC and isentropic eddy mixing are largely suppressed in the lower stratosphere, the stratospheric transport naturally slows down its acceleration following the movement of ϕ_0, as mean AOA anomalies decrease in magnitude (from large negative number to almost zero) over both TTU and polar downwelling region whereas the 'surf zones' (20° – 40°N/S) remain relatively unchanged. Besides, there are two other interesting phenomena worthy of mentioning: (a) the changes of isentropic eddy mixing and mean AOA are quite sensitive to the movement of ϕ_0 across certain critical latitude, since it is clear to observe the significantly different behaviours

between the solid line group and the dash line group, which are differentiated by *Qobs_3gau_15N* and *Qobs_3gau_20N*; (b) near transit phase, for example, in *Qobs_3gau_15N*, the strengthening of BDC has already reduced to a relatively unchanged mode, meaning little acceleration of stratospheric transport due to the diabatic circulation. However, the 15°N centered SST perturbation keeps to excite isentropic eddy mixing in SH (cf. Figure 5.2(c)) so that the transport in lower-stratosphere SH remains accelerated with younger mean AOA (cf. Figure 5.2(e)). The situation at tropopause is generally similar to the one in the lower stratosphere except the anomalies of $\bar{w}^*$ in TTU becomes irregular and the isentropic eddy mixing in the NH tropospheric subtropical jet begins to weaken the in situ transport barrier (cf. Figure 3.4(c)).

Further, the residual vertical velocity $\bar{w}^*$ within TTU (70 hPa, 15°S – 15°N) has been particularly examined using the 'downward control' principle introduced in Section 2.2.2. As Illustrated in Figure 5.3, the residual vertical velocity $\bar{w}^*$ within TTU (bold solid line) monotonically decreases from a positive anomaly (strengthened TTU) to a negative anomaly (weakened TTU), as ϕ_0 continues moving off the equator. This is consistent with the findings in Figure 5.2(a). Moreover, the dynamic-balance derived residual vertical velocity $\bar{w}^*_m$ (dashed line), by applying downward control analysis, and the thermodynamic-balance derived one $\bar{w}^*_Q$ (dot-dashed line) render a relatively consistent downward trend following the northward movement of heating center. This implies the weakening of intensification of TTU is corresponded to a reduction of wave dissipation and it is balanced by a coherent diabatic heating change. The discrepancy between $\bar{w}^*$ and $\bar{w}^*_Q$, in experiments with ϕ_0 restrained in deep tropics (0-10°N), might be caused by the omission of vertical diffusion process in the model. And the incoherence between $\bar{w}^*$ and $\bar{w}^*_m$, in experiments with ϕ_0 shifted close to 30°N,

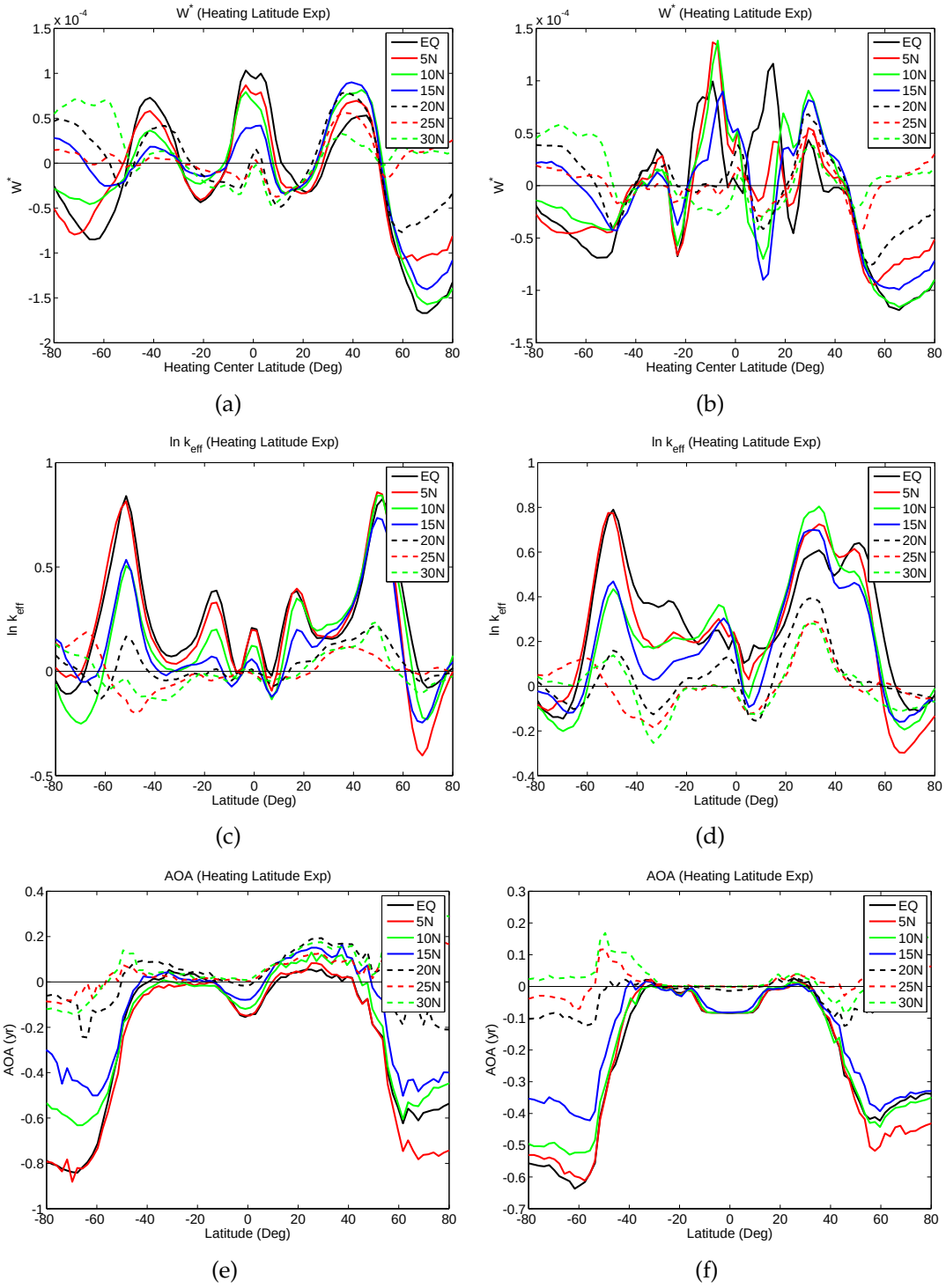

Figure 5.2: Anomalies of (a) residual vertical velocity $\bar{w}^*$ (m/sec) at 100 hPa; (b) $\bar{w}^*$ at 70 hPa; (c) isentropic eddy mixing denoted by logarithm of equivalent length ratio $\ln \tilde{\kappa}_{eff}$ at 100 hPa; (d) $\ln \tilde{\kappa}_{eff}$ at 70 hPa; (e) mean AOA (yr) at 70 hPa; (f) mean AOA at 100 hPa.

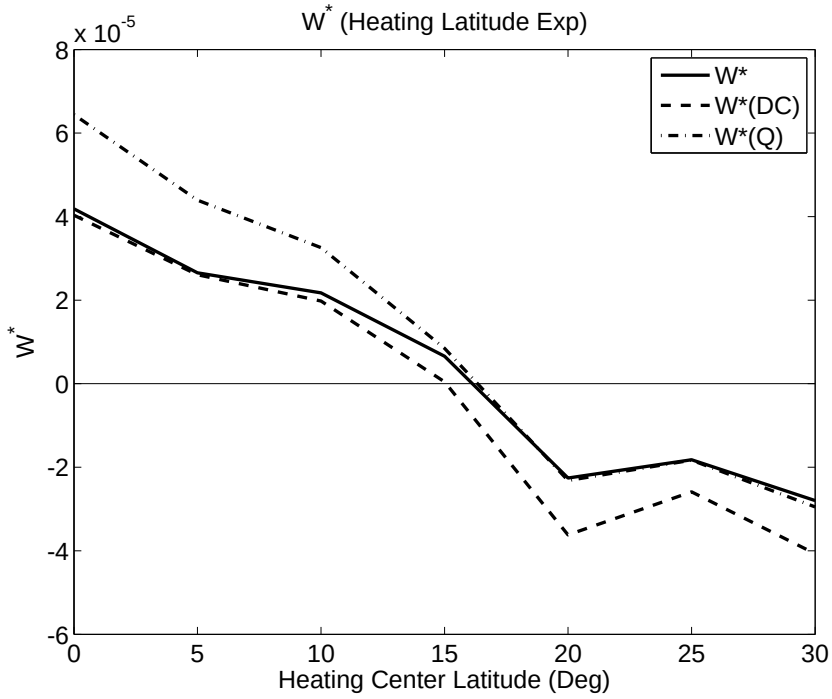

Figure 5.3: Anomaly of residual vertical velocities (unit: m/sec) averaged within the latitudinal range from 15°S to 15°N at 70 hPa for Gaussian-shaped SST perturbation with heating center (ϕ_0) varies from 0 to 30°N (see reference at Table 2.1): definition derived $\bar{w}^*$ (solid line), dynamic balance derived $\bar{w}^*_m$ (dashed line), and thermodynamic balance derived $\bar{w}^*_Q$ (dot-dashed line).

is probably due to the deficiency of temporal sampling frequency of output data (not shown here). Another interesting phenomenon is that: the critical latitude for TTU transit from a strengthening mode into a weakening mode is between 15° and 20°, which also lies in the one for differentiating different reaction patterns of isentropic eddy mixing and mean AOA. Therefore, in terms of varying ϕ_0, BDC and isentropic eddy mixing in the lower stratosphere respond quite consistently.

In order to scrutinize the eddy behaviors further, EP flux divergence (**DF**) and corresponding residual meridional velocity $\bar{v}^*$ are plotted for experiment

Qobs_3gau_15N (cf. Figure 5.4(a) and 5.5(a)), in which the the anomaly of TTU almost disappears, and for experiment *Qobs_3gau_30N* (cf. Figure 5.4(b) and 5.5(b)), in which TTU weakens. Obviously in *Qobs_3gau_15N*, the anomaly of eddies resembles what it is in *Qobs_3gau* in NH but becomes much weaker in SH. Thus, though the significantly intensified wave dissipation in NH (negative **DF**) still induces a strong northward motion, there is no sufficient equivalent southward movement of air in SH to generate pronounced divergence in deep tropics right above the tropopause at 70 hPa, and consequently no intensive TTU strengthening will be observed. As to the experiment *Qobs_3gau_30N*, the anomaly of EP flux divergence, relatively weaker in magnitude though, represents an opposite phase with divergent changes (i.e. reduced wave dissipation) almost everywhere over the lower and middle stratosphere. In current study, the underlying reasons for large domain of suppressed wave dissipation in the stratosphere remain many possibilities, but the resulting reduced divergent residual flows above 70 hPa, according to Equation 2.7a, still helped to explain the weakening of TTU when the center of Gaussian SST perturbation shifts sufficiently northward.

The eddy changes also help to interpret the changes of isentropic eddy mixing near polar night jets for experiment *Qobs_3gau_30N*. With suppressed wave dissipation and intensified zonal winds over the polar night jet region, the isentropic eddy mixing across the polar night jet decreases significantly (cf. Figure 5.2(c), green dashed line), which is consistent with the prediction in Section 4.2.

In all, the latitude of SST perturbation center, as well as its associated size adjustment, apparently affects the physical backgrounds for which eddies generate, propagate, and dissipate. The altered behaviors of eddies further act to im-

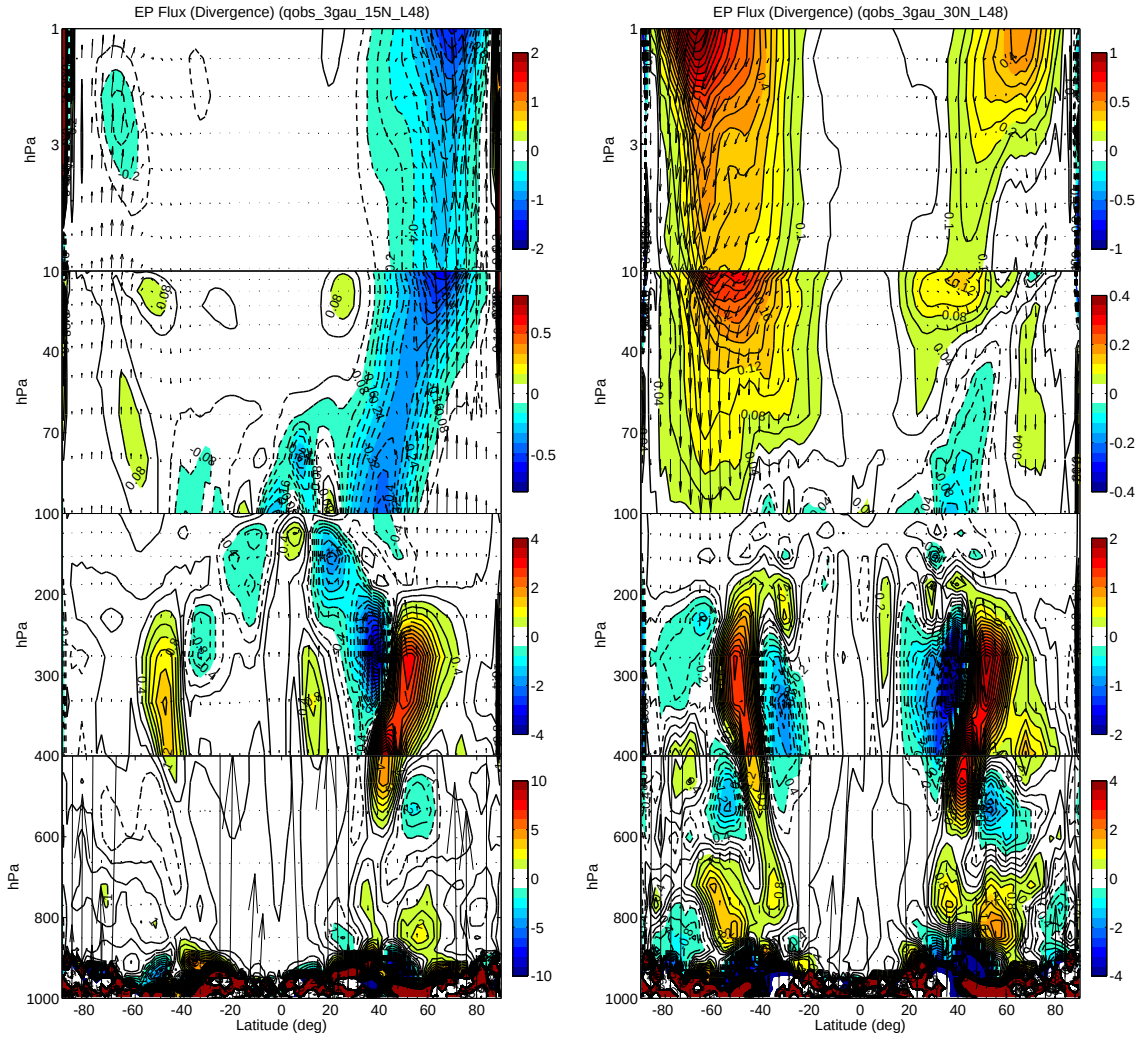

(a) (b)

Figure 5.4: Same as Figure 4.1(a), but for: (a) *Qobs_3gau_15N*; (b) *Qobs_3gau_30N* and the contour interval here alters to 0.05 m sec^{-1}day^{-1} (1-10 hPa), 0.02 m sec^{-1}day^{-1} (10-100 hPa), 0.1 m sec^{-1}day^{-1} (100-400 hPa), and 0.2 m sec^{-1}day^{-1} (400-1000 hPa). Notice the different scaling of coloring between left and right panel.

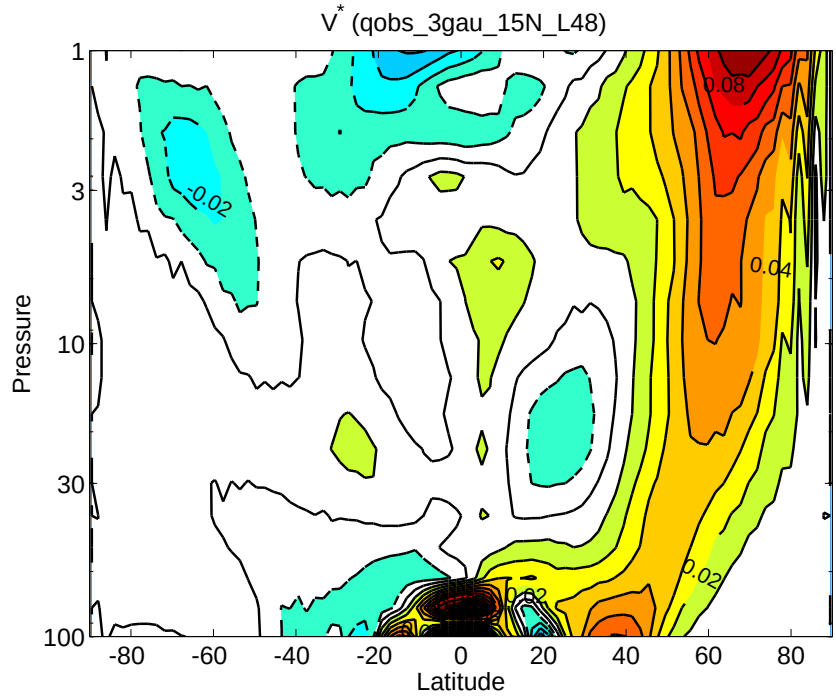

(a)

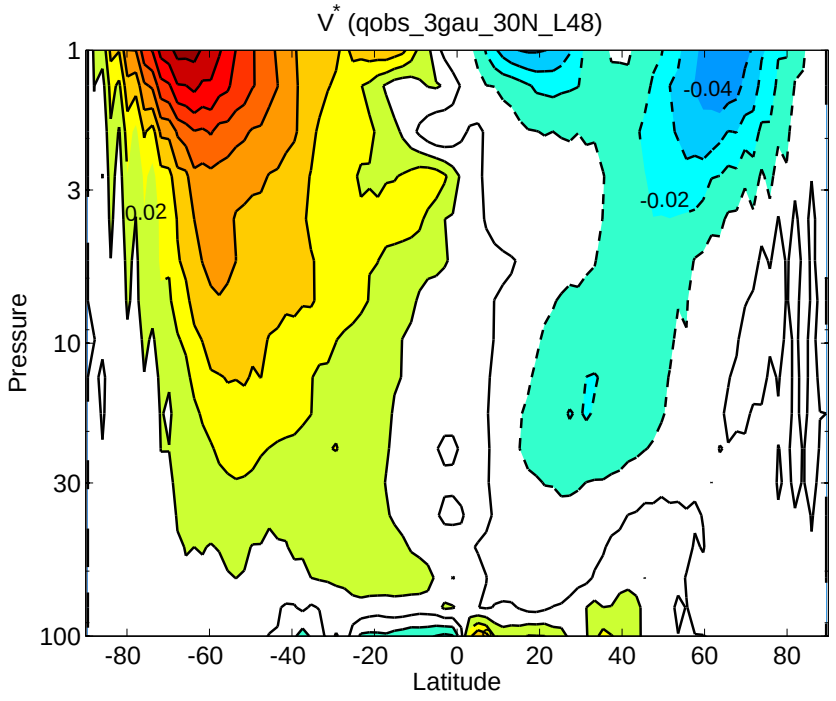

(b)

Figure 5.5: Same as Figure 4.2, but for: (a) *Qobs_3gau_15N*; (b) *Qobs_3gau_30N*.

pact on BDC, isentropic eddy mixing and ultimately produce a structural modification on stratospheric transport. Additionally, the northward movement of heating center, to some extent, represents a quarter of natural SST seasonality, but, of course, this argument is limited by the simultaneous change on size of heating. Hence, to identify which factor is more crucial, latitude or size, a better scheme of simulation design is needed, which is also an interesting topic to explore further in the future.

5.2 Longitudinal Span λ_S

Despite the heating center latitude ϕ_0, the longitudinal span λ_S of SST perturbation could exert impacts on stratospheric transport as well. Plus, it is common in nature to observe SST anomaly in different longitudinal broadness. For example, the discrepancy between major El Niños and minor El Niños. Thus in this section, the Gaussian SST perturbation applied in sensitivity experiments has its heating center latitude ϕ_0 fixed at the equator, but with the longitudinal span λ free to vary.

Figure 5.6 shows changes of zonal mean zonal wind, zonal mean temperature and stratospheric residual stream function after the longitudinal span λ_S of SST perturbation has been changed to 15° in *Qobs_3gau_X15* and 150° in *Qobs_3gau_X150* respectively. With relatively narrower equatorial heating in *Qobs_3gau_X15*, the magnitude of atmospheric responses are not as strong as the ones in *Qobs_3gau*, but the spatial patterns are generally retained. One exception is the spatial preference on BDC strengthening in the lower stratosphere, which have been seen in the NH in *Qobs_3gau_15N*. However, for *Qobs_3gau_X150*

in which the SST perturbation is tremendously broad, atmosphere apparently reacts very differently. The subtropical jets strengthen instead of becoming weaken. The polar night jets are still decelerated but less in magnitude, while the relatively weak wind zones connecting polar night jets and subtropical jets are now turning stronger with faster westerly flows. Consistent with the deceleration of polar night jets, polar vortices continue warming. Lower stratosphere cooling and upper troposphere warming are also observed, but the latter discernibly becomes much broader, covering almost the entire troposphere above 700 hPa. The most essential change related to current study is the change of BDC. Here, BDC strengthening is much deeper into the middle stratosphere and the magnitude of intensification in the tropical region increases significantly.

Further, the systematically changes of BDC, isentropic eddy mixing and mass transport due to the longitudinal expansion of SST perturbation are examined in Figure 5.7. Coherent with the BDC strengthening deduced from a sneak peek at *Qobs_3gau_X15* and *Qobs_3gau_X150*, the residual vertical velocity $\bar{w}^*$ increases monotonically in tropics at 70 hPa (regardless of the irregularity at the equator). However, the changes of $\bar{w}^*$ in extratropical regions are no longer following the same pattern: with a secondary strong strengthening of BDC centered at approximately 50°N/S in experiments having narrow heatings in contrast with a minor strengthening at high latitudes right after the major tropical strengthening in experiments having broad heatings. Despite the difference of BDC strengthening spatial pattern, the BDC itself is generally becoming more and more intensified following the increase of λ_S. As to isentropic eddy mixing at 70 hPa, the prevailing of westerly flows over connection zones, bridging tropospheric subtropical jets and stratospheric polar night jets, largely blocks it. While the continuing weakening of polar night jets on their poleward

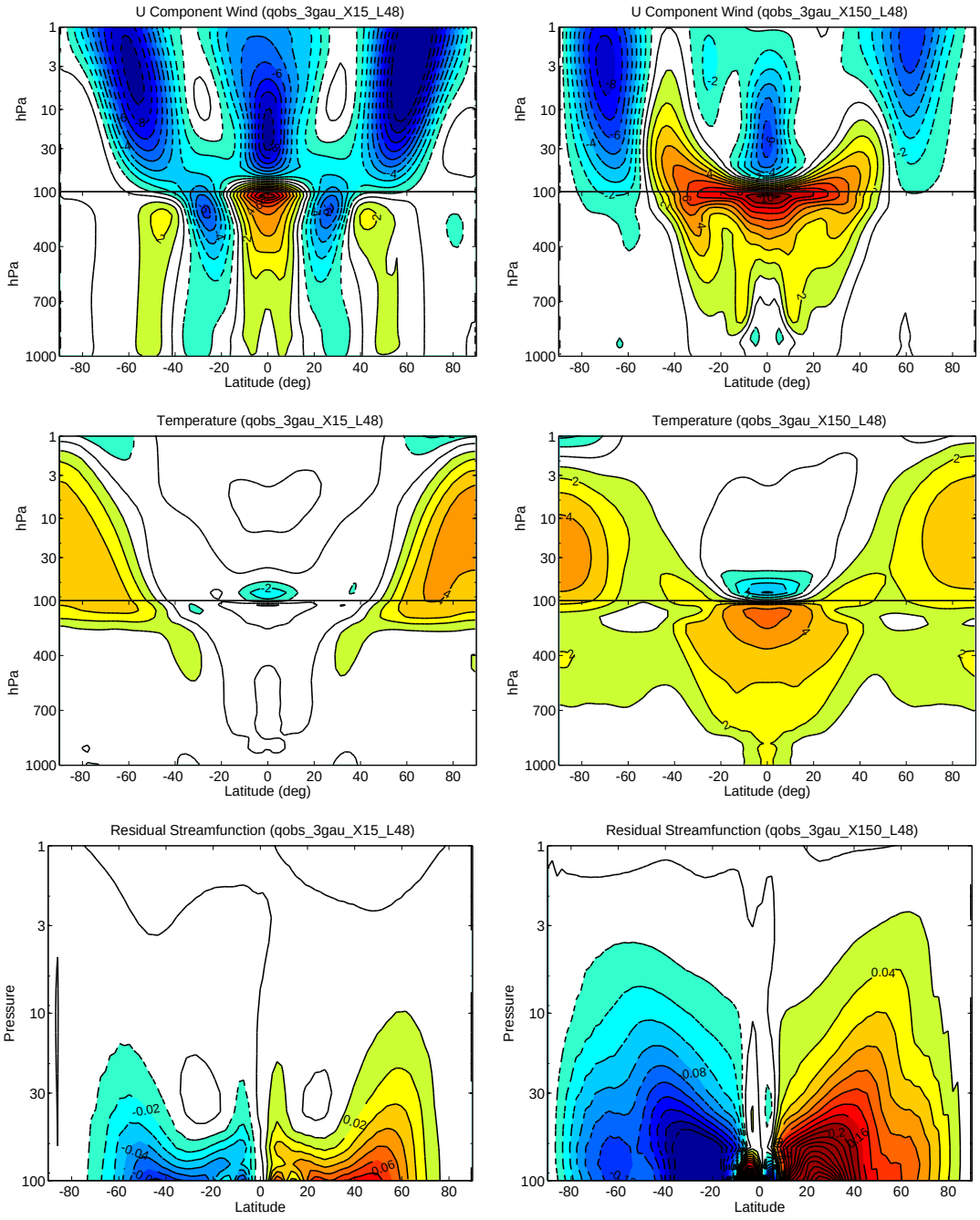

Figure 5.6: Similar to Figure 5.1, expect these plots are for experiments with varying longitudinal span λ_S: (left column) *Qobs_3gau_X15*, (right column) *Qobs_3gau_X150*.

flanks stimulates the isentropic eddy mixing centered at approximately 60°N/S. Thanks to the strong intensification of BDC, the mean AOA at 70 hPa persists to become younger conquering the negative influence from slow-down isentropic eddy mixing in middle latitudes. The curling back of mean AOA anomaly at $40° - 60°$N/S in experiments with $\lambda_S = 150$ and ∞ could be attributed to both the spatial alteration of BDC strengthening and the suppression of isentropic eddy mixing over connection zones. At 100 hPa, the TTU continues strengthening with increased λ_S except the very deep tropics portion, and the extratropical variations generally reproduce the pattern at 70 hPa, but with a relatively weak magnitude. Isentropic eddy mixing increases dramatically in deep tropics with broader heating induced deep convection, compensating the transport tardiness associated with weakening of in situ upwelling. Over extratropical region, it oppositely decreases in middle latitudes partially due to the corresponding strengthening of in situ zonal winds. Hence, the BDC and isentropic eddy mixing in middle latitudes respond oppositely in ventilating polar region at tropopause level, and this competition can be detected by observing the largest negative mean AOA anomaly in experiments with medium broadness of heatings.

In Section 4.1, it is clear that the changes of BDC associating with an equatorial heating is hightly correlated to the mechanic forcing by eddies. And in Section 5.1, we have shown that the variation of BDC following the variation of ϕ_0 of SST perturbation is consistent with the variation of eddy forcing as well. Do eddies play the same role in affecting BDC, with varied λ_S? Yes, in FIgure 5.8, similar to experiments with varied heating center latitude ϕ_0, the general agreement of residual vertical velocity $\bar{w}^*$ derived from three approaches (definition, downward control and thermodynamic balance) demonstrates current

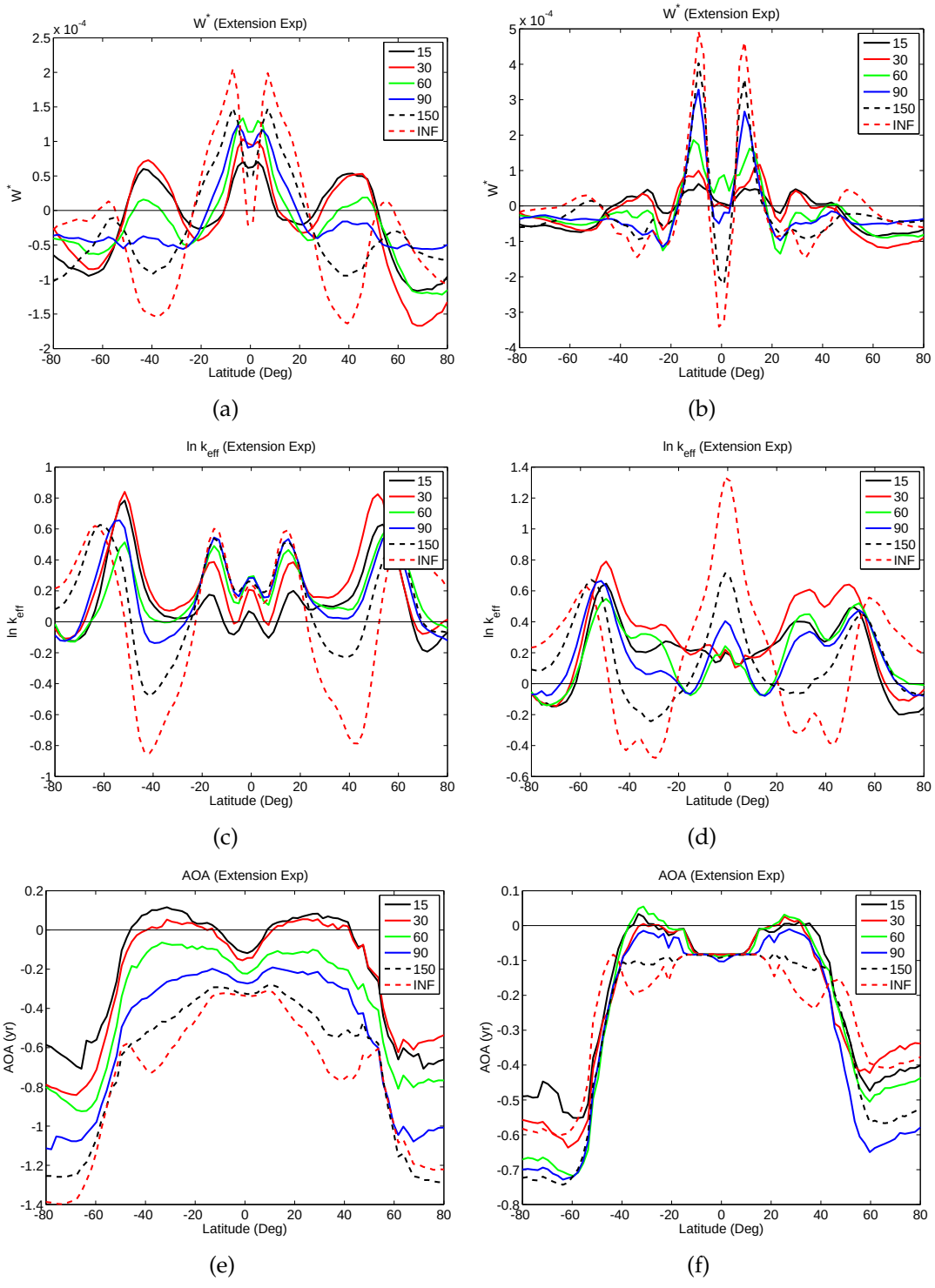

Figure 5.7: Anomalies of (a) residual vertical velocity $\bar{w}^*$ (m/sec) at 100 hPa; (b) $\bar{w}^*$ at 70 hPa; (c) isentropic eddy mixing denoted by logarithm of equivalent length ratio $\ln \tilde{\kappa}_{eff}$ at 100 hPa; (d) $\ln \tilde{\kappa}_{eff}$ at 70 hPa; (e) mean AOA (yr) at 70 hPa; (f) mean AOA at 100 hPa.

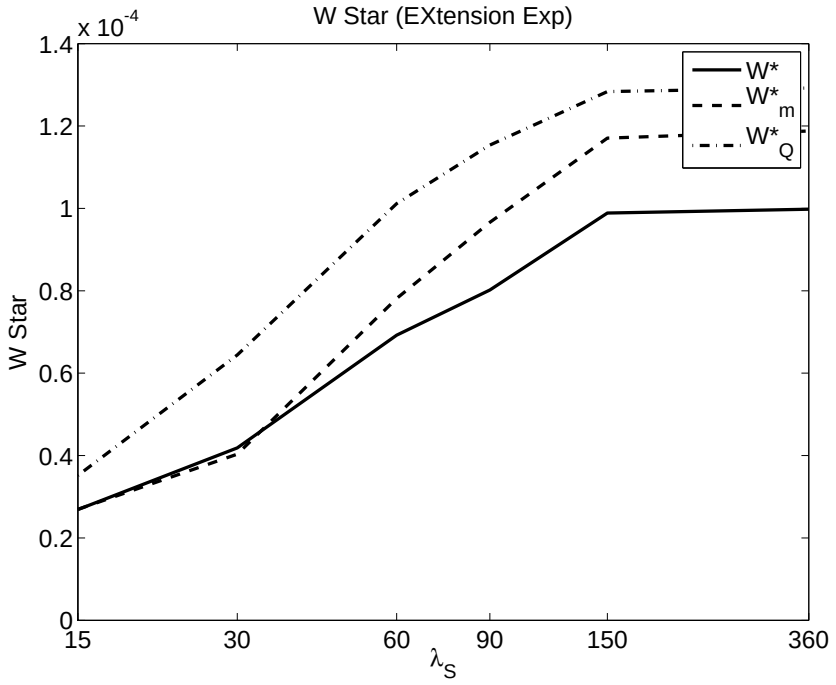

Figure 5.8: Analogous to Figure 5.3 except the varying quantity here is replaced by the longitudinal span λ_S and the heating center is kept at the equator (i.e. $\phi_0 = 0$).

monotonic strengthening of TTU, with increasing longitudinal span λ_S, is mechanically driven by the monotonic increase of eddy dissipation and is balanced by local diabatic heating adjustment as well.

The elongation on longitudinal span λ_S will bring two aspects of changes to the prescribed SST perturbation. First, following a smaller Gaussian decay rate longitudinally, more SST perturbation will be induced into the model globally. Second, since the length of any loop along longitudinal direction is spatially limited, expanding SST perturbation longitudinally will modify its zonal asymmetry. For example, if the λ_S goes to positive infinity, there will be no decay of SST perturbation longitudinally and the heating itself becomes purely zonally symmetric. To quantify the magnitude and zonal asymmetry of SST perturbation, the global averaged SST perturbation, defined by Equation 5.1, and the

variance of SST perturbation along the equator σ^2, defined by Equation 5.2, are applied respectively.

$$\langle T \rangle = \frac{\int_{-\frac{\pi}{2}}^{\frac{\pi}{2}} 2\pi a \bar{T}_{anmly}(\phi) \cos\phi \, d\phi}{4\pi a^2} \tag{5.1}$$

$$\sigma^2 = \frac{1}{N-1} \sum_{n=1}^{N} \left(T_{anmly}(\lambda(n), \phi) - \bar{T}_{anmly}(\phi) \right)^2 \tag{5.2}$$

Here $\bar{T}_{anmly}$ is the zonal mean SST perturbation and it is a function of latitude ϕ. n is the numbering of grid point along longitudinal direction in the model and N is its upper limit.

From Table 5.1, it is clear that, as longitudinal span λ_S of SST perturbation extending, the magnitude of surface forcing, denoted as $\langle T \rangle$, increases monotonically while its zonal asymmetry, denoted as σ^2 displays a curve with a maximum at $\lambda_S = 60°$. Considering the anomaly of residual vertical velocity $\bar{w}^*$ within TTU increases monotonically with the extension of longitudinal span λ_S, it is apparent that, through the competition between magnitude and zonal asymmetry of SST perturbation, the former acts more efficiently than the latter in the process of determining TTU strengthening.

Denoted as the anomaly of EP flux divergence (**DF**), Figure 5.9 depicts the eddy changes in selected experiments, in which the longitudinal span λ_S of SST perturbation are set as 15°, 60° and 150° respectively. With longitudinal span λ_S increases, the climatological wave dissipation (cf. Figure 4.1(b)) in subtropical region (20° - 40°) at middle/upper troposphere (200 hPa - 400 hPa) are suppressed, partially due to the decrease of eddy generation at lower levels (600-800 hPa). Simultaneously, as zonal asymmetry peaks at longitudinal span λ_S

Table 5.1: Magnitude (denoted as the global averaged SST $\langle T \rangle$) and zonal asymmetry (denoted as the latitudinal variance of SST perturbation along the equatorial loop σ^2) of SST perturbation in each associated experiment, affiliating with the corresponding tropical domain (±15°) averaged residual vertical velocity at 70 hPa.

Name	Residual Vertical Velocity Anomaly $\bar{w}^*$	Global Averaged SST Anomaly $\langle T \rangle$	Variance of Equatorial SST Perturbation σ^2
	(mm)	(K)	(K^2)
Qobs_3gau_X15	.0269	.0505	0.4200
Qobs_3gau	.0419	.1011	0.7421
Qobs_3gau_X60	.0692	.2021	1.0923
Qobs_3gau_X90	.0802	.3018	1.0668
Qobs_3gau_X150	.0989	.4600	0.5539
Qobs_3ygau	.1225	.6842	0

being close to 60°, the zonal asymmetry associated stationary eddies have their greatest magnitude of generation in deep tropics in *Qobs_3gau_X60*, and subsequently the overall wave dissipation near tropical tropopause also peaks in *Qobs_3gau_X60* with this medium λ_S. However, the persistent flatting of latitudinal gradient of zonal winds $\frac{\partial \bar{u}}{\partial \phi}$ (due to the strengthening of subtropical jets with broader heating) assist to amplify the effects of reduced equatorial drags after λ exceeding 60°, and maintain the monotonic increase of TTU strengthening. In the meanwhile, without greatly intensified dissipation at tropical tropopause, more equatorial eddies are capable to propagate vertically into the higher stratosphere, and continue to result in strong eddy dissipation in subtropical lower and middle stratosphere. It is exactly these eddy dissipation that trigger the lowermost branch of BDC developing deeper and possessing a much

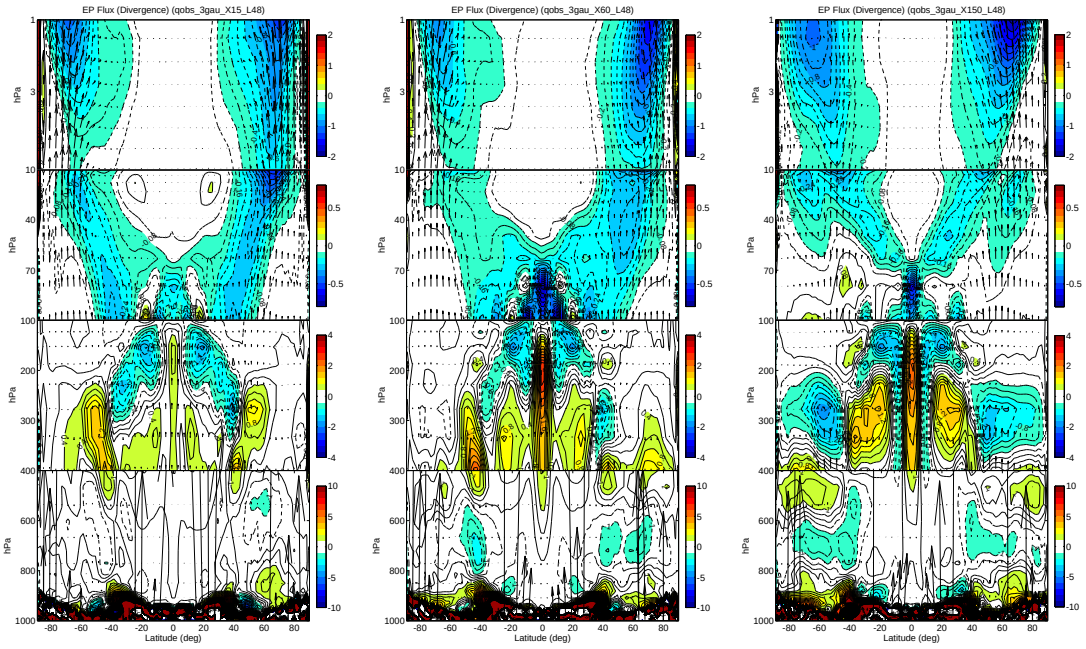

(a) (b) (c)

Figure 5.9: Same as Figure 4.1(a) except the anomaly field is plotted for experiments: (a) *Qobs_3gau_X15*, (b) *Qobs_3gau_X60* and (c) *Qobs_3gau_X150* respectively.

stronger tropical strengthening in experiments with a sufficient broad heating. Finally, shown in Figure 5.9(c), the strengthening of wave dissipation in middle and high latitudes (> 40°) at middle/upper troposphere (200 hPa - 400 hPa) reinforces the climatological eddy dissipation zones, blocks amounts of synoptic eddies from propagating vertically into stratosphere, and ultimately result in the high-latitude BDC strengthening becoming minor, which are consistent with what we have seen in Figure 5.6(f).

As to isentropic eddy mixing, in *Qobs_3gau_X150*, the qualitatively unchanged eddy dissipation in mid-latitude lower stratosphere, cooperating with the acceleration of in situ westerly zonal winds, suppresses the isentropic eddy mixing. However, at the upper flank of subtropical jets at tropopause, the eddy dissipation has been increased, acting against to a decline of isentropic eddy

mixing (cf. Figure 5.7(d)). Apparently, the strengthening of subtropical jets overcomes the increase of local eddy dissipation, and continues to suppress the isentropic eddy mixing there.

For longitudinal span λ_S, its modification will not only refresh the overall magnitude but also the zonal asymmetry of the forcing, and both of them tend to adjust the BDC and the isentropic eddy mixing. Generally speaking, the former works more effectively than the latter in determining the strength of BDC. With SST perturbation becoming longitudinally broader, the BDC consistently develops deeper and stronger, while isentropic eddy mixing in the lower stratosphere (70 hPa) and at tropopause (100 hPa) over subtropical or middle latitudes are turning weaker. Through the competition between these two processes, the BDC dominates in the lower stratosphere (70 hPa) displaying a monotonic decrease of polar mean AOA, while, at tropopause (100 hPa), BDC and isentropic eddy mixing are so close that they have to switch their superiority over the other from case to case.

5.3 BDC versus isentropic eddy mixing

From Section 5.1 and Section 5.2, it has been shown that any modification on heating center latitude ϕ_0 or longitudinal span λ_S of SST perturbation could affect the stratospheric transport through simultaneously changing the BDC and the isentropic eddy mixing. However, which one is the dominant? BDC or isentropic eddy mixing? In this section, simple statistical methods are applied to unveil the answer.

Before mapping the critical zones for BDC and isentropic eddy mixing in af-

fecting the UTLS mass transport, mean AOA in the NH polar vortex and mean AOA on the poleward flank of NH subtropic jet are chosen particularly to have a skim on the competing relationship between these two opponents. A simple linear regression is applied between the mean AOA at selected locations noted above and the potential influential factor, BDC or isentropic eddy mixing. Theoretically, with a stronger BDC, the mass transport in the stratosphere expects to run faster, reducing the mean AOA in the polar vortex. Same theorem applies to the isentropic eddy mixing considering the mean AOA at high-latitude lower stratosphere as noted above. Hence, for both BDC and isentropic eddy mixing, a negative slope is expected in scatter plots shown as Figure 5.10, regardless of how the SST perturbation is added. However, in practice, these two processes could become opponents in determining the mass transport in the UTLS region. Once one process overwhelms in the competition against the other, the losing process will then be free from obeying a negative slope. Here in the NH polar vortex, the transport, conveying tracers into it, is strongly dominated by the BDC. Because the negative slopes involving BDC are qualitatively identical, insensitive to type variation of SST perturbation, and particularly the isentropic eddy mixing loses the battle by displaying a positive slope in experiments with varied λ_S. On the other hand, in regions highly affiliating to the NH subtropical jet close to tropopause, isentropic eddy mixing is undoubtedly important in determining the transport across the strong zonal flows, by consistently displaying negative slopes in experiments with varied ϕ_0 and varied λ_S. However, the discrepancy between extent of negative inclines, as well as the negative slope involving BDC in experiments with varied ϕ_0, indicates the superiority of isentropic eddy mixing over the BDC in determining the mass transport near NH subtropical jet is not that clear.

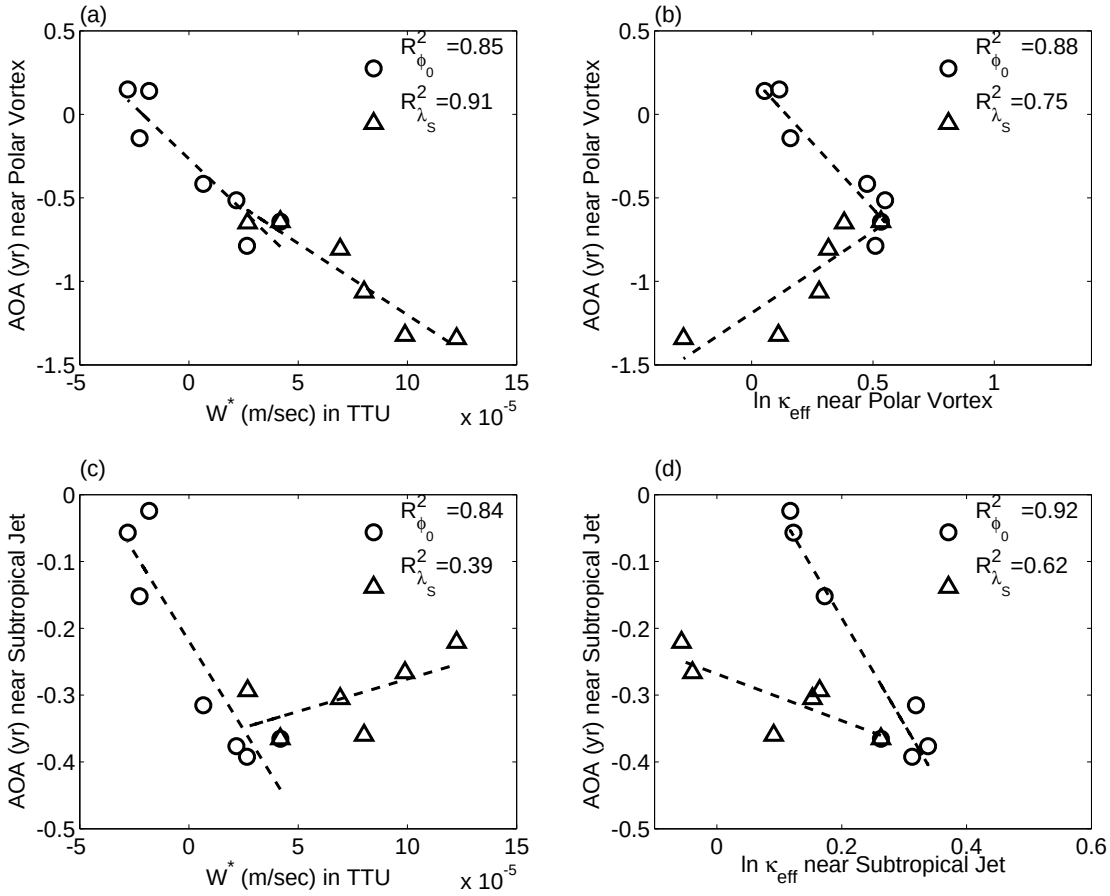

Figure 5.10: Scatter plots examining the correlation between: (a) anomalies of BDC and anomalies of transport throughout the polar vortex; (b) anomalies of isentropic eddy mixing near the polar night jet and anomalies of transport throughout the polar vortex; (c) anomalies of BDC and anomalies of transport near the subtropical jet; and (d) anomalies of isentropic eddy mixing and anomalies of transport both near the subtropical jet. Here, the anomalies of BDC are denoted by residual vertical velocity $\bar{w}^*$ (m/sec) anomalies in the TTU (15°S–15°N, 70 hPa); the anomalies of isentropic eddy mixing are assessed by logarithm of equivalent length ratio $\ln \tilde{\kappa}_{eff}$ changes near the northern subtropical jet (20°N – 40°N, 100-300 hPa) and the polar night jet (40°N – 60°N, 50-70 hPa) separately; and, at last, the transport anomalies are quantified through mean AOA (yr) anomalies near the subtropical jet (40°N – 60°N, 100-200 hPa) and in the polar vortex (60°N – 80°N, 40-60 hPa). Experiments with varying ϕ_0 or λ_S are marked as $\circ$ or $\triangle$ respectively. The coefficients of determination R^2 associating with the experiments, either by varying ϕ_0 or by λ_S, are both given in the upright corner legends.

Further examination shows that the results in Figure 5.10 could be highly sensitive to the choice of average box on regression-involved properties. In order to skip this dependence and further view geographically which portion of mass transport in the UTLS is strongly influenced by BDC, or by isentropic eddy mixing, correlation between BDC (or isentropic eddy mixing) and mean AOA is calculated at every grid point. Analogous to the setting used in FIgure 5.10, the intensity of BDC is denoted by the residual vertical velocity $\bar{w}^*$ anomalies within TTU (15°S – 15°N, 70 hPa) and the strength of isentropic eddy mixing is denoted by the equivalent length ratio $\tilde{\kappa}_{eff}$ anomalies near the NH subtropical jet (20°N – 40°N, 100-300 hPa). All perturbation experiments are included to form the data series at each model grid point. As illustrated in Figure 5.11(a), mass transport through almost the entire lower stratosphere is highly correlated to the changes of BDC, and the correlation coefficient increases negatively along the path of BDC — tropical upwelling and polar downwelling in the polar vortices. Moreover, the high correlation zones over higher latitudes in the upper troposphere are produced by the coincident changes of isentropic eddy mixing due to either acceleration of poleward flank of subtropical jets in experiments with varied ϕ_0 or increased in situ eddy dissipation in experiments with varied λ_S. And these correlation zones may disappear when more types of SST perturbation are applied. As to isentropic eddy mixing near the NH subtropical jet, the influence is quite local along the equatorward flank of NH subtropical jet, while the high positive correlation zones in tropical stratosphere are induced by the oppositely varied TTU: in experiments with varied ϕ_0, weakening of the NH subtropical jet motivates in situ isentropic eddy mixing while TTU becomes weaker following the northward movement of heating center; in experiments with varied λ_S, strengthening of the NH subtropical jet suppresses the in situ

isentropic eddy mixing while TTU becomes stronger with more total heating induced by SST perturbation with larger longitudinal broadness.

In all, through the competition between BDC and isentropic eddy mixing, the BDC overwhelms in the lower stratosphere, particularly along its path, in determining the mass transport, while isentropic eddy mixing is more locally effective.

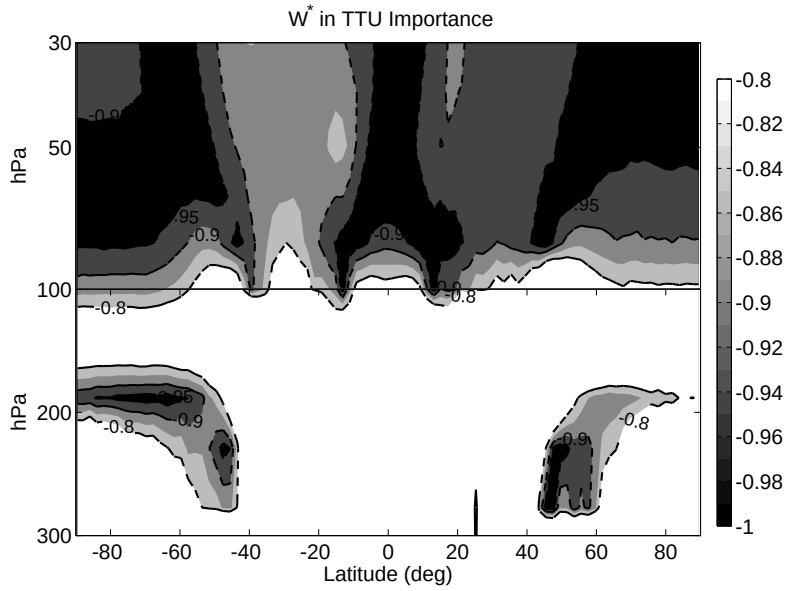

(a)

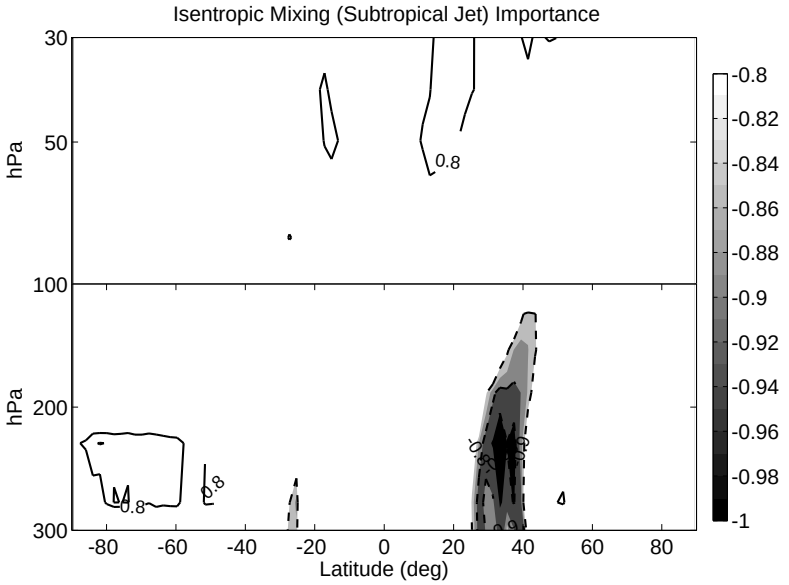

(b)

Figure 5.11: Correlation mapping between (a) BDC and UTLS mean AOA; (b) isentropic eddy mixing near the NH subtropical jet and UTLS mean AOA. The denotation for strength of BDC and isentropic eddy mixing near the NH subtropical jet follow the same definition in Figure 5.10. Correlation coefficients smaller than -0.8 are shaded with a 0.05 interval, and contours are applied for the ones having absolute value of 0.8, 0.9, 0.95 respectively (solid: positive; dash: negative).

CHAPTER 6

DISCUSSION

In previous chapters, the stratospheric transport has been documented to be intensified after an equatorial SST perturbation is imposed. Further, the transport will become less intensified if the heating center latitude ϕ_0 moves away from the equator or continue stronger if the heating longitudinal span λ_S expands. Dynamic diagnosis argues this intensification of stratospheric transport is highly attributed to the variaiton of eddy dissipation. One of the motivation in current study is to provide dynamic information on the projection of stratospheric chemistry under the impact of varied SST. As noted at the beginning of Chapter 1, ozone is one of the chemical species that mostly discussed in the stratosphere and is still worthy of noting given the results of current study.

It has been shown that the changes of BDC dominates the mass transport in the lower stratosphere (see Section 5.3). And with warmed SST perturbation, the BDC is projected to be strengthened, and consequently tends to accelerate the meridional transport of ozone by shifting abundant generated tropical ozone into polar region (Dobson 1956). This is definitely beneficial in another way for the polar ozone recovery predicted in WMO's report (World Meteorological Organization (WMO)/United Nations Environment Programme (UNEP) 2007) besides the reduced emission of anthropogenic Ozone Depletion Substances (ODS). In the model study of Calvo et al. (2010), stratospheric ozone concentration is also displayed with a negative trend in the tropics along with a positive trend in high latitudes during warm ENSO events, consistently indicating a strengthening of poleward ozone transportation in the stratosphere. Hence, despite the complexity of many other factors, the equatorial SST increase

solely is supposed to trigger an intensified BDC through eddy dissipation, and further is expected to drive the meridional motion within the BDC in accelerating the recovery process of polar stratospheric ozone. Moreover, in the awareness of the sign alteration of anomaly of BDC, as well as the NH polar mean AOA, while moving the heating center sufficiently off the equator (cf. Figure 5.2), it is expected to foresee a seasonal cycle of ozone recovery through oscillation of transport intensity. However, the actual variability embedded within the process of ozone recovery is much more complicated than just considering transport variation induced by SST perturbation. Waugh et al. (2009) suggests the recovery of stratospheric ozone in current century would also be significantly affected by GHG induced global warming, and the recovery itself is represented with abundant regional diversity. Moreover, variation on chemical sources/sinks of ozone is also inevitable when projecting future's ozone recovery. Hence in order to elucidate this issue in further concrete details, it is necessary to consider sophisticated model simulation in future research, especially with chemistry module encompassed.

Other than the chemistry effects induced by stratospheric transport under SST perturbation, there are also many other aspects of deficits involved through current research. First, the temporal resolution of data mentioned in Section 2.1. In current study, the strategy of four times daily data works qualitatively well representing the diurnal variability with equatorial heating imposed. However, the momentum budget, resolved in current temporal sampling, is no longer strictly balanced when heating center latitude ϕ_0 shifts into subtropical region. Calculating flux terms instantaneously within the model at a temporal interval of 20 minutes could highly increase the sampling frequency and it has been shown promisingly effective to address this issue in a better quality. Second,

the vorticity balance utilized for zonal asymmetry analysis referring to Equation 2.12. As noted in Section 4.1.2, it indeed provides some intuitive information about the mechanism of eddies' impacts on the TTU. However, unlike the 'downward control' principle shown in Equation 2.10, it lacks explicit linkages to eddy forcing and further is unable to supply as quantitative assessment in current form. The bright side is, analogous to 'downward control' principle, Equation 2.12 is originated from the momentum equation as well. Thus, reasonable transformation could also reconstruct the vorticity balance equation into a form that explicitly bonds the vertical velocity (within TTU) with eddy dissipation and hence provides as an effective tool for dynamic diagnostics upon a spatial view of full three dimensional data (without preliminary zonal average). Though not fully applied in current study, it could be still a meaningful direction of amelioration in future research.

About the sensitivity experiments, for both heating center latitude ϕ_0 and longitudinal span λ_S runs, the total energy induced is not conserved. Hence, it is hard to argue, in current study, whether the variation of stratospheric mass transport is mainly due to the spatial modification of SST perturbation or the accompanying energy changes. Nevertheless, the discussion, shown as Table 5.1, at least gives us some hint that probably the induced total energy is more efficient than the spatial pattern of SST perturbation to excite changes within stratospheric mass transport. Moreover, further experiment designs keeping induced total energy perturbation conserved would also help to elucidate this issue.

CHAPTER 7

CONCLUSION

Back to the three questions mentioned at the end of Chapter 1, through current study, the questions are at least partially answered based on the aqua-planet model simulation.

(a) The stratospheric transport will be strengthened after an equatorial SST perturbation is imposed. It is attributed to a simultaneous acceleration of BDC and intensification of isentropic eddy mixing near stratospheric polar night jets, working consistently to weaken transport barriers and reduce the mean AOA in the higher-latitude lower stratosphere. However, the relative contribution from each of the process, BDC or isentropic eddy mixing, to the strength of stratospheric transport, particularly the one within lower stratosphere, is hard to distinguish by looking at this equatorial heating experiment only. Further, a warm ENSO event in reality could promote the mass transport in the stratosphere following current simulation projection.

(b) With heating center latitude ϕ_0 moving poleward, both BDC and isentropic eddy mixing reduce their extent of strengthening, which slows down the acceleration of stratospheric transport. With heating longitudinal span λ_S becoming broader, BDC continues being stronger while isentropic eddy mixing near the polar night jets are suppressed, but overall, the stratospheric transport is still accelerated due to the strong dominance of BDC. Moreover, by analyzing the consistency of behaviors from BDC and isentropic eddy mixing under different types of SST perturbation, it has shown that: BDC affects the mass transport over almost the entire lower stratosphere, with its strongest impact residing within its path, while the effects of isentropic eddy mixing near the

NH subtropical jet is locally restrained.

(c) The strengthening of BDC is highly attributed to the dissipation of eddies originated from both tropics and extratropics. Increased equatorial SST tends to generate more stationary eddies in deep tropics through deep convection and simultaneously suppress transient eddy dissipation in extratropical regions, allowing more eddies propagating vertically into the stratosphere. On the other hand, the in situ weakly superrotation of zonal winds provides a favorable environment for vertical propagation of tropical stationary eddies until encountering a relative westerly jet in the upper troposphere close to the tropopause. Eddies start to dissipate above the critical level and the dominance of EP flux convergence, associating with transient eddies passing the weakened dissipation zone in upper troposphere from extratropics, undoubtedly excites residual meridional motion. It is indeed the strengthened meridional flow that acts as a mechanic torque driving BDC accelerated. The strength of isenropic eddy mixing highly depends on the in situ eddy dissipation and the in situ zonal flow. Generally, large isentropic eddy mixing will occure at places in which eddy dissipation is strong and zonal flows are weak. Moreover, the dynamic relationship between BDC and eddies, and relationship between isentropic mixing and eddies are consistently valid in case with changed ϕ_0, or λ_S.

BIBLIOGRAPHY

Andrews, D. G., J. R. Holton, and C. B. Leovy, 1987: *Middle Atmosphere Dynamics*. Academic Press, 489 pp.

Austin, J., J. Wilson, and F. Li, 2007: Evolution of water vapor concentrations and stratospheric age of air in coupled chemistry-climate model simulations. *J. Atmos. Sci.*, **64**, 905–921.

Availone, L. M. and M. J. Prather, 1996: Photochemical evolution of ozone in the lower tropical stratosphere. *J. Geophys. Res.*, **101**, 1457–1461.

Brewer, A. W., 1949: Evidence for a world circulation provided by the measurements of helium and water vapor distribution in the stratosphere. *Q. J. Roy. Meteor. Soc.*, **75**, 351–363.

Butchart, N. and A. A. Scaife, 2001: Removal of chlorouorocarbons by increased mass exchange between the stratosphere and troposphere. *Nature*, **410**, 799–802.

Calvo, N., R. R. Garcia, W. J. Randel, and D. R. Marsh, 2010: Dynamical mechanism for the increase in tropical upwelling in the lowermost tropical stratosphere during warm ENSO events. *J. Atmos. Sci.*, **67**, 2331–2340.

Charney, J. G. and P. G. Drazin, 1961: Propagation of planetary-scale disturbances from the lower into the upper atmosphere. *J. Geophys. Res.*, **66**, 83–109.

Chen, G., R. A. Plumb, and J. Lu, 2010: Sensitivities of zonal mean atmospheric circulation to SST warming in an aqua-planet model. *Geophys. Res. Lett.*, **37**, L12 701.

Deckert, R. and M. Dameris, 2008: Higher tropical SSTs strengthen the tropical upwelling via deep convection. *Geophys. Res. Lett.*, **35**, L10 813.

Delworth, T. L., et al., 2006: GFDL's CM2 Global Coupled Climate Models. Part I: Formulation and Simulation Characteristics. *J. Climate*, **19**, 643–674.

Dobson, G. M. B., 1956: Origin and distribution of the polyatomic molecules in the atmosphere. *Proc. Roy. Soc. London*, **236A**, 187–193.

Edmon Jr, H. J., B. J. Hoskins, and M. E. McIntyre, 1980: Eliassen-Palm cross sections for the troposphere. *J. Atmos. Sci.*, **37**, 2600–2616.

Engel, A., et al., 2008: Age of stratospheric air unchanged within uncertainties over the past 30 years. *Nat. Geosci.*, **2**, 28–31.

Fu, Q., S. Solomon, and P. Lin, 2010: On the seasonal dependence of tropical lower-stratospheric temperature trends. *Atmos. Chem. Phys.*, **10**, 2643–2653.

Garcia, R. R. and W. J. Randel, 2008: Acceleration of the BrewerDobson circulation due to increases in greenhouse gases. *J. Atmos. Sci.*, **65**, 2731–2739.

Garcia, R. R., W. J. Randel, and D. E. Kinnison, 2011: On the Determination of Age of Air Trends from Atmospheric Trace Species. *J. Atmos. Sci.*, **68 (1)**, 139–154.

Garny, H., M. Dameris, W. J. Randel, G. E. Boderker, and R. Deckert, 2011: Dynamically forced increase of tropical upwelling in the lower stratosphere. *J. Atmos. Sci.*, **68**, 1214–1233.

Gerber, E. P., 2012: Stratospheric versus Tropospheric Control of the Strength and Structure of the BrewerDobson Circulation. *J. Atmos. Sci.*, **69 (9)**, 2857–2877.

Gill, A. E., 1980: Some simple solutions for heatinduced tropical circulation. *Q. J. Roy. Meteor. Soc.*, **106**, 447–462.

Hall, T. M. and R. A. Plumb, 1994: Age as a diagnostic of stratospheric transport. *J. Geophys. Res.*, **99 (D1)**, 1059–1070.

Haynes, P. and E. Shuckburgh, 2000a: Effective diffusivity as a diagnostic of atmospheric transport 1. Stratosphere. *J. Geophys. Res.*, **105 (D18)**, 22 777–22 794.

Haynes, P. and E. Shuckburgh, 2000b: Effective diffusivity as a diagnostic of atmospheric transport 2. Troposphere and lower stratosphere. *J. Geophys. Res.*, **105 (D18)**, 22 795–22 810.

Haynes, P. H., C. J. Marks, M. E. Mcintyre, T. G. Shepherd, and K. P. Shine, 1991: On the "Downward Control" of extratropical diabatic circulation by eddy-induced mean zonal forces. *J. Atmos. Sci.*, **48**, 651–678.

Held, I. M., 1999: Equatorial superrotation in Earth-like atmospheric models. *Bernhard Haurwitz Memorial Lecture*, American Meteorological Society.

Holton, J. R., 2004: *An Introduction to Dynamic Meteorology*. 4th ed., Academic Press, 535 pp.

Holton, J. R., P. H. Haynes, M. E. Mcintyre, A. R. Douglass, and R. B. Rood, 1995: Stratosphere-troposphere exchange. *Rev. Geophys.*, **33**, 403–439.

Kerr-Munslow, A. M. and W. A. Norton, 2006: Tropical wave driving of the annual cycle in tropical tropopause temperatures. Part I: ECMWF analyses. *J. Atmos. Sci.*, **63**, 1410–1419.

Li, F., R. S. Stolarski, and P. A. Newman, 2009: Stratospheric ozone in the post-CFC era. *Atmos. Chem. Phys.*, **9**, 2207–2213.

Matsuno, T., 1966: Quasi-geostrophic motions in the equatorial area. *J. Meteorol. Soc. Jpn.*, **44**, 25–43.

Nakamura, N., 1996: Two-dimesional mixing, formation, and permeability diagnosed in an area coordinate. *J. Atmos. Sci.*, **53 (11)**, 5002–5020.

Neale, R. B. and B. J. Hoskins, 2000: A standard test for AGCMs including their physical parametrizations: I: The proposal. *Atmos. Sci. Lett.*, **1**, 101–107.

Norton, W. A., 2006: Tropical wave driving of the annual cycle in tropical tropopause temperatures. Part II: model results. *J. Atmos. Sci.*, **63**, 1420–1431.

Olsen, S. C., C. A. McLinden, and M. J. Prather, 2001: Stratospheric N_2O-NO_y system - testing uncertainties in a three-dimensional framework. *J. Geophys. Res.*, **106**, 28 771–28 784.

Plumb, R. A. and J. Eluszkiewicz, 1999: The BrewerDobson circulation : dynamics of the tropical upwelling. *J. Atmos. Sci.*, **56**, 868–890.

Randel, W. J., R. R. Garcia, N. Calvo, and D. Marsh, 2009: ENSO influence on zonal mean temperature and ozone in the tropical lower stratosphere. *Geophys. Res. Lett.*, **36**, L15 822.

Randel, W. J., R. R. Garcia, and F. Wu, 2008: Dynamical balances and tropical stratospheric upwelling. *J. Atmos. Sci.*, **65**, 3584–3595.

Simpson, I. R., T. G. Shepherd, and M. Sigmond, 2011: Dynamics of the lower stratospheric circulation response to ENSO. *J. Atmos. Sci.*, **68**, 2537–2556.

Thompson, D. W. J. and S. Solomon, 2005: Recent stratospheric climate trends as evidenced in radiosonde data: Global structure and tropospheric linkages. *J. Climate*, **18**, 4785–4795.

Ueyama, R. and J. M. Wallace, 2010: To what extent does high-latitude wave

forcing drive tropical upwelling in the BrewerDobson circulation? *J. Atmos. Sci.*, **67**, 1232–1246.

Uppala, S. M., et al., 2005: The ERA-40 re-analysis. *Quarterly Journal of the Royal Meteorological Society*, **131**, 2961–3012.

Waugh, D. W., 2009: Atmospheric dynamics: The age of stratospheric air. *Nat. Geosci.*, **2**, 14–16.

Waugh, D. W., L. Oman, S. R. Kawa, R. S. Stolarski, S. Pawson, A. R. Douglass, P. A. Newman, and J. E. Nielsen, 2009: Impacts of climate change on stratospheric ozone recovery. *Geophys. Res. Lett.*, **36 (3)**, L03 805.

World Meteorological Organization (WMO)/United Nations Environment Programme (UNEP), 2007: Scientific Assessment of Ozone Depletion: 2006. Tech. Rep. 50, World Meteorological Organization, 572 pp.

Yang, H., K. Tung, and E. Olaguer, 1990: Nongeostrophic Theory of Zonally Averaged Circulation. Part II: Eliassen-Palm Flux Divergence and Isentropic Mixing Coefficient. *Journal of Atmospheric Sciences*, **47 (2)**, 215–241.

Yulaeva, E. and J. R. Holton, 1994: On the cause of the annual cycle in tropical lower-stratospheric temperatures. *J. Atmos. Sci.*, **51**, 169–174.